Experimental investigation of a closed vertical cylinder-shaped fish cage in waves

Yugao Shen[a,b,*], Reza Firoozkoohi[a,d], Marilena Greco[a,b,c], Odd M. Faltinsen[a,b]

[a] *Department of Marine Technology, Norwegian University of Science and Technology (NTNU), Trondheim, NO-7491, Norway*
[b] *Centre for Autonomous Marine Operations and Systems (AMOS), NTNU, Trondheim, NO-7491, Norway*
[c] *CNR-INM, Institute of Marine Engineering, Rome, Italy*
[d] *Sintef Ocean, Trondheim, Norway*

Abstract

Wave-induced response of a closed floating fish cage consisting of a vertical circular cylinder with an external toroidal floater is studied theoretically and experimentally. A main purpose was to investigate how the internal sloshing would influence the global response of the cage, the interior wave elevation and also the mean drift loads. An ocean basin laboratory was used in order to minimize tank wall effects. An optical system involving eight markers was used to obtain experimental values for radial elastic deformations of the cylindrical part. The closer a coupled natural period between body motions and sloshing is to a corresponding natural sloshing period, the more nonlinear sloshing can be. In the examined case, the highest coupled natural period between surge, pitch and sloshing is 0.8 times the highest natural sloshing period. Linear potential flow theory can, in general, explain experimental transfer functions of rigid-body motions and sloshing due to rigid-body motions obtained by both regular wave and truncated white noise tests. Theoretical second order mean wave drift forces based on a rigid body and potential flow agree also well with experimental results. Resonant 3D sloshing was excited due to ovalizing hydroelastic structural modes in both regular waves and white-noise tests. The closeness between the corresponding structural and sloshing frequencies caused large response. A linear hydroelastic analysis based on WAMIT and LS-DYNA could partly explain the response. Parametric resonant pitch response occurred experimentally at large wave periods partially due to in and out of water motion of portions of the floater and was explained by treating the pitch as uncoupled motion modeled by the Mathieu equation. The pitch motion predicted by linear potential flow theory was, in general, unsatisfactory when the floater was partly out of the water occasionally.

Keywords: Global response, mean drift forces, hydroelasticity, regular wave tests, white-noise tests

*Corresponding author
Email address: shenyugaonuaa@gmail.com (Yugao Shen)

1. Introduction

There exists a variety of floating fish farms with net cages. Since salmon lice and pollution is of major concern, closed fish farms have recently been proposed to have a better control over the internal water quality. Depending on the material, closed fish cages can be divided into flexible membrane cages (e.g. fabric), semiflexible/elastic cages (e.g., GRP), and rigid cages (e.g., concrete or steel). They have typically a vertical symmetry axis at rest with a circular shape in the waterplane. Examples on diameters in the water plane are 40-50m. A pump system is needed for water exchange in the tank, and waste must be removed from the tank. Typical steady flow velocities caused by the pumping system are 0.2-0.4 m/s. Since the water inside a closed tank causes statically destabilizing roll and pitch moments, torus-shaped floaters around the fish cage have been proposed. The hydrodynamic flow associated with closed fish cages differs strongly from net cages. Potential flow effects with wave generation caused by the cage dominate for closed fish cages, while viscous flow is dominant for net cages. This has consequences both for the wave induced response and mooring system analysis.

Wave-induced sloshing (interior resonant wave motion) becomes an issue in closed fish cages as well known in many engineering applications (Faltinsen and Timokha, 2009). Lateral tank excitations involving the lowest natural sloshing frequency is of primary sloshing concern for a rigid tank. When the lateral tank motion is prescribed and harmonic, the liquid motion at the lowest natural sloshing frequencies can dependent on the excitation level be strongly nonlinear. Free-surface nonlinearities can develop three dimensional (3D) liquid motion. For instance, forced horizontal motion of a vertical circular tank in the vicinity of the lowest sloshing frequency can cause swirling or irregular chaotic 3D motions that depend on the forcing amplitude and the liquid depth. The interior wave motion becomes secondary for larger wavelength-to-diameter ratio. However, it matters for roll and pitch that the interior free surface will then remain nearly horizontal.

When the tank is part of a structure moving in incident waves, the sloshing behavior differs from that induced by prescribed tank motion. For instance, if a rigid body with a tank is restrained to only move in surge, the body amplitude will according to linear theory and steady-state conditions be zero when the wave frequency is equal to a natural sloshing frequency $\omega_{2i-1}, i = 1, 2, ..$ associated with antisymmetric natural sloshing modes. The latter is a consequence of that the magnitude of the surge added mass A_{11}^{slosh} associated with sloshing is infinite at the natural sloshing frequencies. In the case of coupled surge-sloshing system, the maximum response is associated with coupled surge-sloshing natural frequencies $\omega_{\mathrm{coupl},2i-1}$. The latter are solutions of the equation $M_t + M_l + A_{11}^{slosh}(\omega) = 0$ when the surge restoring force is negligible. Here M_t is the sum of the body mass and surge added mass associated with the external flow. Furthermore, M_l is the liquid mass in the tank. The reason for the coupled surge-sloshing frequencies $\omega_{\mathrm{coupl},2i-1}$ is the negative values of A_{11}^{slosh}, which can be expressed as an infinite sum where each term is a positive constant times $1/\left(\omega_{2i-1}^2 - \omega^2\right)$. It means that A_{11}^{slosh} can be positive or negative depending on the frequency. The consequence is, e.g., that $\omega_{\mathrm{coupl},1} > \omega_1$. If the coupled natural frequency $\omega_{\mathrm{coupl},1}$ is very close to the natural sloshing frequency ω_1, the sloshing response can be violent. Faltinsen and Timokha (2021) studied this problem systematically for

a body with a rectangular tank in 2D flow conditions and compared with model tests by Rognebakke and Faltinsen (2003). They introduced the ratio M_t/M_l as a parameter. They found that $\omega_{\text{coupl},1}/\omega_1$ increased with decreasing M_t/M_l and liquid depth-to-tank breadth ratio and that $\omega_{\text{coupl},1}/\omega_1$ tended to 1 (without reaching 1) with increasing M_t/M_l and liquid depth-to-tank breadth ratio. We can generalize these findings by studying the response in the vicinity of any natural sloshing frequency and incorporating any relevant body motions in finding the coupled natural frequency. For a rigid body, this means either surge and pitch or sway, roll and yaw. Rigid-body heave can not excite sloshing according to linear theory. The fact that a closed fish cage can be flexible and has a vertical symmetry axis at rest introduces, in particular, concern for the lowest natural sloshing frequency with an ovalizing radial mode shape.

While nonlinearities may matter for sloshing, the exterior potential flow can in many cases be based on linear potential flow theory of incompressible water, for instance by Shen et al. (2020). Corrections due to viscous flow separation may matter as damping. Wave drift forces are needed for the mooring analysis, which can be based on a second-order potential flow analysis for the exterior flow problem. The coupled effect of interior water behavior on the body motions must be accounted for. Current can have a non-negligible effect on wave drift forces. Since potential-flow wave drift forces are related to waves generated by the structure, care is needed in model tests to minimize tank-wall interference. Second-order slowly varying loads in irregular sea causing resonant surge, sway and yaw must also be considered as it is done for moored floating offshore structures with spread mooring systems. Neither the latter effect nor the effect of current are studied in this paper.

Although studies on sloshing and the coupled motions of ships are highly relevant, for instance those by Malenica et al. (2003), Rognebakke and Faltinsen (2003), Newman (2005) and Kim et al. (2007), there are still some differences between a ship and a closed cage. For instance a ship normally possesses larger M_t/M_l than the closed cage. Also, a closed cage can be more flexible and hydroelasticity may matter, with more modes relevant than those typically important for ships. An experimental study on the wave induced responses of a closed flexible structure was performed by Lader et al. (2017). Linear response of a 2D closed flexible fish cage in waves was investigated numerically by Strand and Faltinsen (2019). The motion of the membrane was represented as the sum of rigid body motions and Fourier series with zero displacement at the attachment to the floater. Linear frequency-domain potential flow theory of incompressible water was used both for the interior and external flows. Strong coupling between elastic modes and rigid-body motions was observed. The approach was extended to investigate linear wave-induced dynamic structural stress of a 2D semi-flexible closed fish cage by Strand and Faltinsen (2020). They compared a quasi-static analysis with a fully coupled hydroelastic analysis to examine the soundness of assuming that the stresses in the structure are quasi-static and concluded that whether a hydroelastic analysis is necessary depending to the stiffness of the structure. Kristiansen et al. (2018) presented scaled physical experiments of a floating rigid closed-cage model in waves. Two model configurations were tested to investigate the coupling effects of the contained water on the rigid body motions: one with the model filled with water and one with the contained

water replaced by fixed weights. The results showed that the influence of sloshing on the rigid body motion was significant. Mean wave loads were also affected by sloshing. The tests were performed in a towing tank and wave reflections from the side tank walls were found to have large influence on the mean wave drift force. This phenomenon was also illustrated by Zhao et al. (1988) who presented experimental results and theoretical analysis for a hemisphere in a conventional towing tank at zero and small forward speed.

In the present paper, we present results from model tests of a Froude-scaled closed cage in regular and truncated white noise waves. The tests were conducted in a large ocean basin to minimize the disturbances from side-wall reflections and served as a follow up of the experiments performed by Kristiansen et al. (2018). The paper is organized as follows. A description of the experimental set up is given at first. Next, the technique to post-process the experimental data, including extracting rigid body motions and elastic deformations is explained. In the last part, relevant experimental results are given and analyzed. The focus is on the transfer functions of rigid body motions, radial elastic deformations, internal sloshing and mean wave drift forces. Numerical results from a linear potential flow solver WAMIT are also provided for comparison. The effect of hydroelasticity is studied by coupling WAMIT with the structural analysis software LS-DYNA (Hallquist, 2007). Furthermore, parametric pitch resonance is discussed.

2. Experimental setup

Model tests were performed in the Ocean Basin Laboratory at the Marine Technology Center in Trondheim. The basin has an overall length of 80 m and width of 50 m. The depth can vary between 0-10 m by an adjustable floor and was set to 5 m. All values presented hereafter are in model scale unless otherwise noted.

The physical model used in the experiments included a vertical cylindrical closed cage moored by four horizontal mooring lines, as shown in Figure 1. A model test scale ratio of 1:27 and Froude scaling with geometric similarity was in mind. Two Cartesian right-handed coordinate systems were implemented in the model tests, one global system $Oxyz$ referred to the basin and one local system fixed to the model. The origin of the former is in the plane of undisturbed free surface with vertical z-axis positive upwards through the center of the cage in calm water and positive x towards the wavemaker. The center of the model was located at the basin center when at rest. The local body-fixed coordinate system coincides with the global coordinate system in still water. Details of the system, including the cage model, the mooring lines, and the arrangement of the various measurement instruments are introduced below.

2.1. Cage model description

Photo of the cage model from the front camera is presented in the left of Figure 1. A sketch of the model and detailed dimensions are illustrated in Figure 2. The model contained a vertical circular cylinder with draft h =0.75 m and outer diameter $D = 2R = 1.5$ m. The side wall of the cylindrical cage was made of polycarbonate resin (Lexan) with thickness t_c= 5 mm. The resulting diameter of the internal tank becomes

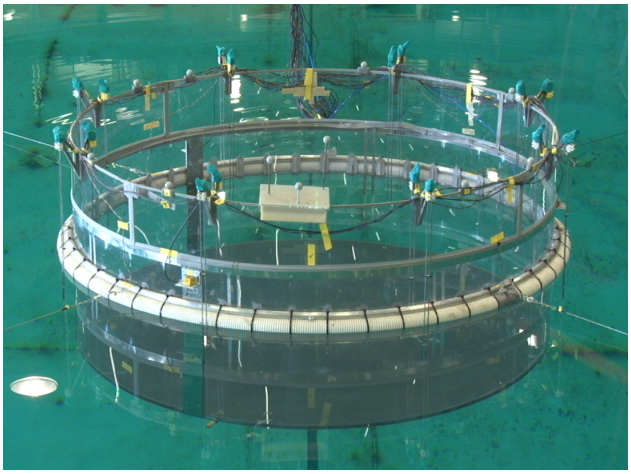

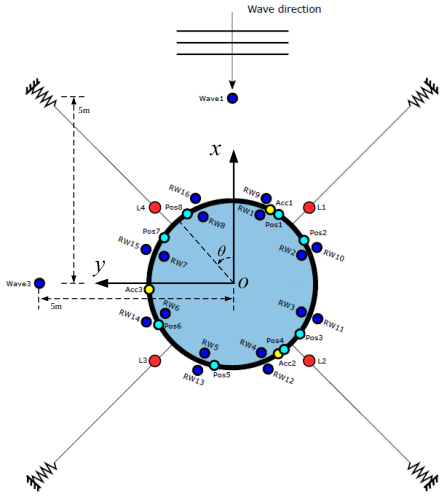

Figure 1: Left: front-camera photo of the physical set-up. Right: sketch of the instrumentation setup from top view. Blue circles: internal and external wave probes. Sky-blue circles: optical positioning markers. Yellow circles: accelerometers. Red circles: force transducers.

$D_t = 2R_t = 1.49$ m. The tank bottom contains two layers, a round PVC disk on top to prevent leakage of internal fluid and an Divynicell plate below to add buoyancy, both having a thickness of 10 mm, leading to a tank depth $h_t = 0.73$ m. A semi-submerged torus shaped floating collar was attached to the outside of the cylindrical cage, providing additional static stability and buoyancy. The floating collar was made of plastic electrical tube with cross-sectional diameter $d_f = 0.05$ m. Two massive aluminum rings were added above and below the floating collar to reduce the flexibility of the cage, each with a cross-sectional diameter of 20 mm. Three groups of vertical aluminum plates (both inside and outside of the tank) were used to connect the polycarbonate plate, with 120 degrees between each. Two perpendicular steel square tubes were installed exterior to the cage bottom to reduce the deformation of the bottom plates. The positions of the vertical aluminum plates and bottom steel tubes relative to the incident wave are illustrated in Figure 3, showing an asymmetry of the model with respect to the $x-z$ plane. The freeboard of the model was increased to h_u=0.35 m to prevent spilling of water in high pitch/roll motions by gluing two polycarbonate plates with an horizontal curved aluminum plate. The main particulars of the model are given in Table 1. The metacentric height given in the table is defined as $GM = C_{55}/(\rho g \nabla)$, with C_{55}, ρ, g, ∇ the restoring coefficient for pitch motion, density of fresh water, gravitational acceleration and water displacement of the model, respectively. C_{55} is evaluated (see Faltinsen and Timokha (2009)) as

$$\begin{aligned} C_{55} &= \rho g \nabla z_b - M g z_g - M_l g z_{g,l} \\ &+ \rho g \int\limits_{A_{W,c}} x^2 ds + \rho g \int\limits_{A_{W,f}} x^2 ds - \rho g \int\limits_{A_{W,l}} x^2 ds \end{aligned} \tag{1}$$

where M is the mass of the dry model (dry cage + floating collar), z_g and z_b are the corresponding center of gravity (COG) and center of buoyancy (COB), respectively. M_l is the mass of internal water and $z_{g,l} = -h_t/2$

is the corresponding center of gravity. $A_{W,c}$, $A_{W,f}$ and $A_{W,l}$ are the waterplane area of the dry cage, floating collar and internal water, respectively. The main reason for positive C_{55} comes from the second last term, i.e., the restoring provided by the floating collar. The sum of the other terms equals approximately zero, indicating that the model is not statically stable without the floating collar.

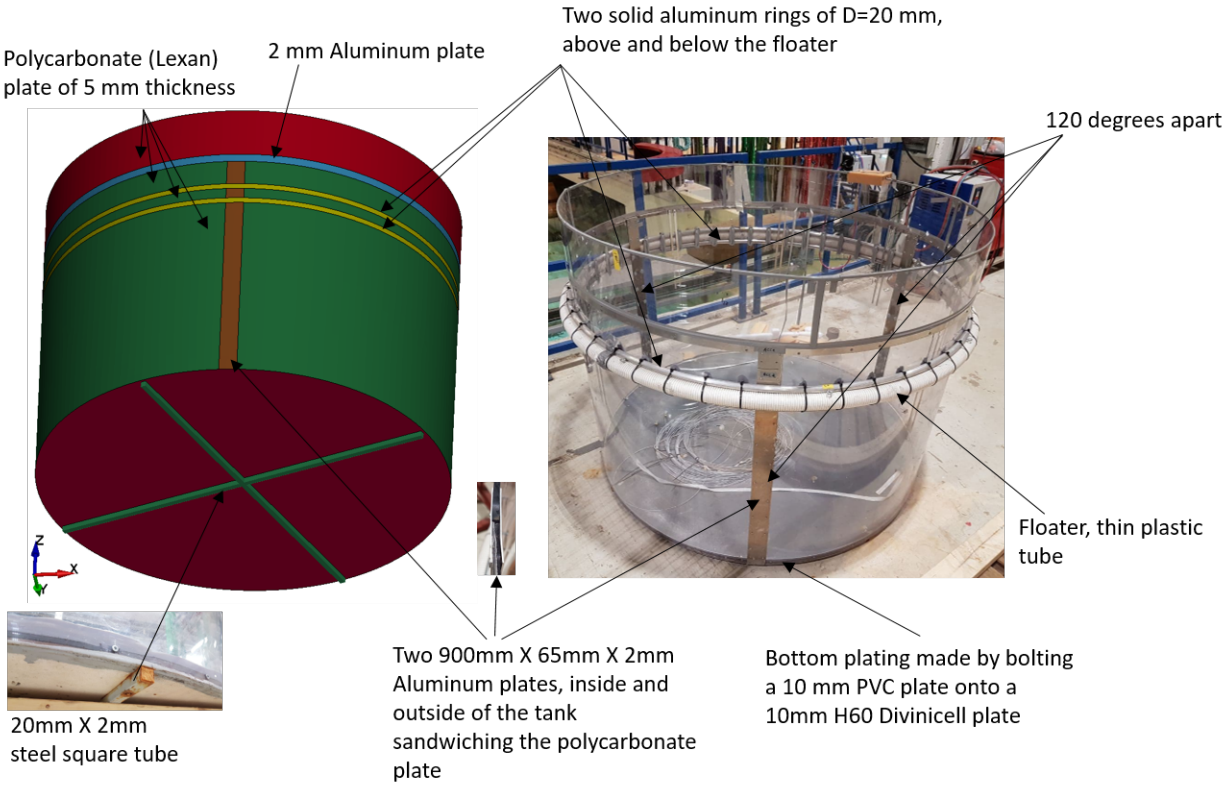

Figure 2: Left: simplified cage model as used in FEM, including the aluminum rings, bottom steel tubes and aluminum plates. Right: photo of the dry cage model.

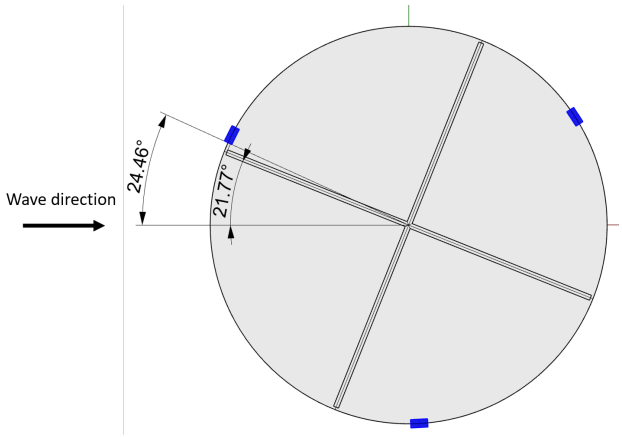

Figure 3: Positions of the vertical aluminum plates and bottom steel tubes relative to the incident wave (bottom view). The blue filled rectangles are the cross sections of the vertical aluminum plates.

Table 1: Parameters of the cage model.

Parameter	**Symbol**	**Dimension**	**Unit**
Diameter	D	1.5	m
Draft	h	0.75	m
Freeboard	h_u	0.35	m
Mass	M	69.0	kg
Center of gravity (COG)	z_g	-0.360	m
Center of buoyancy (COB)	z_b	-0.374	m
Moment of inertia x-axis	I_{xx}	25.86	kgm^2
Moment of inertia y-axis	I_{yy}	25.86	kgm^2
Moment of inertia z-axis	I_{zz}	31.98	kgm^2
Metacentric height	GM	0.054	m

2.2. Mooring system description

The cage model was moored with four mooring lines in the horizontal plane, evenly distributed with 90° between each, see Figure 1. Each of the four mooring lines was attached far away directly to horizontal free-hanging coil springs. The far away ends of the front two mooring lines (L1 and L4 in Figure 1) were elevated 1 m above the calm water surface while the aft two lines (L2 and L3 in Figure 1) were elevated to 0.6 m to avoid contact with water and disturbance of waves during the tests. The stiffness of each coil spring was 60 N/m, yielding an equivalent stiffness $k_s = 169.7$ N/m in x and in y directions for the system. Tension in each mooring line was measured by an uni-axial load-cell that connected the mooring line to the cage. A pretension of $F_{pre} = 45$ N was applied to all mooring lines to avoid them going slack during testing. Since the mooring lines considered are quite long, approximately 33 m each, the small height difference in the far away ends will cause a negligible static pitch. The pretension in the mooring lines nevertheless will provide an additional equivalent pitch restoring coefficient $C_{55,p}$, expressed as $C_{55,p} = F_{pre} \cdot D$. The restoring coefficient for pitch in Equation 1 is corrected by accounting for also the contribution of the mooring lines. The natural periods caused by the mooring system in surge and sway are much larger than our examined wave period range and have, therefore, negligible effect on our studied steady-state response in regular waves.

2.3. Instrumentation

The parameters of interest were global body motions, internal sloshing and mooring loads. The motions were measured using an optical positioning system (Qualisys Oqus) where the position of markers mounted on the model was tracked from camera images. Eight markers (Pos1-8 in Figure 1) were installed along the perimeter of the cage model at freeboard level, i.e., h_u=0.35 m, such that also eventual flexible radial deformations of the cage could be detected. The accuracy of the motion measured by each individual marker

was 0.2 mm. This means a relative error of 0.02 in the experimental transfer functions when the incident wave amplitude is 1 cm. The marker positions with respect to the positive x-axis are provided in the left subtable of Table 2. A set of three markers was also installed for 6 degree-of-freedom rigid-body motions tracking, see the white box installed at the freeboard of the cage in the left of Figure 1. The rigid body motions measured with the three markers may be biased if the cage experiences elastic vibrations, as the setup can not distinguish the rigid motions from elastic vibrations. Wave induced accelerations of the model were measured by three accelerometers mounted on the cage side wall and could serve as a benchmark check of the measured motions from the markers. Detailed arrangement of the markers and accelerometers is illustrated in the right of Figure 1.

Table 2: Marker positions (left) and wave gauge positions (right) θ with respect to positive x-axis and anticlock-wise positive, as defined in Figure 1.

Name	**Position** $\theta[^\circ]$
Marker 1	327.9
Marker 2	301.4
Marker 3	233.9
Marker 4	216.4
Marker 5	167.0
Marker 6	118.7
Marker 7	54.6
Marker 8	32.2

Name	**Position** $\theta[^\circ]$
RW1, RW9	338.3
RW2, RW10	293.3
RW3, RW11	248.3
RW4, RW12	203.3
RW5, RW13	158.3
RW6, RW14	113.3
RW7, RW15	68.3
RW8, RW16	23.3

The model was also fitted with pairs of internal and external conventional wave probes, distributed radially at eight positions along the side wall with a radial distance $0.05R$ from the cage wall. This means that the local wave elevation at the tank was measured in the body-fixed reference frame. Sloshing of the contained water inside the cage model was measured by the internal eight wave probes (RW1-8) while the wave elevation outside was captured by the external eight wave probes (RW9-16). The wave gauge positions with respect to the positive x-axis are provided in the right subtable of Table 2. Two more wave probes were installed 5 m away from the model to measure the front and side wave field, named Wave1 and Wave3 in Figure 1. Prior to testing, the wave field was calibrated without the presence of the model and an additional wave probe denoted Wave2 was intalled at the center position of the model. All data acquisition was performed with a sampling frequency of 200 Hz. Filtering of measured data was performed using an anti-aliasing filter at 50 Hz. Tests were recorded by three video cameras (front, top and side) above the water surface and one camera under the water surface.

2.4. Test conditions

The model was tested in regular waves and truncated white-noise waves. The regular wave tests were performed at a fixed wave steepness $H/\lambda = 1/60$, with H as the wave height and λ as the wave length. In total 24 wave periods were considered varying from 0.6 s and 1.7 s. It means that the corresponding wavelength-to-diameter ratio λ/D changes from 0.38 to 3.0. The full scale wave height was within 0.25 m - 2.03 m, covering the sea conditions from small exposure to heavy exposure, according to the Norwegian aquaculture site classification shown in Table 3. One more test with $T = 2.5$ s and $H = 0.163$ m was also conducted to examine the response of the cage in high exposure sea state. A series of additional tests were performed at higher wave steepness $H/\lambda = 1/45$. The regular wave tests were performed to obtain approximately 2.3 minutes (12 minutes full-scale) data.

In addition, two series of truncated white-noise tests were executed to obtain continuous transfer functions within a given frequency region. The term truncated white noise is used to describe a band limited white noise spectrum, i.e. a square spectrum with nearly equal energy for all frequencies within the upper and lower bounds, and with zero energy outside the bounds. In the tests, the lower and upper period region were 0.577 s (3 s full-scale) and 3.85 s (20 s full-scale) and two significant wave heights were considered, in particular $H_s = 0.037$ m (1 m full-scale) and 0.074 m (2 m full-scale). Hereafter the truncated white-noise tests will be mentioned as white-noise tests. The white-noise tests were conducted to obtain a 34.6 minutes (3 hours full-scale) realization of the spectrum.

Table 3: Norwegian aquaculture site classification for waves and current (StandardNorge, 2009). H_s: significant wave height; T_p: peak period; U_∞: current velocity. It is assumed irregular waves for each wave class. If regular wave is considered, the standard says that the corresponding wave height H can be assumed to be 1.9 times the significant wave height.

Wave	H_s(m)	T_p(s)	**Exposure**	**Current**	U_∞(m/s)	**Exposure**
A	0.0 - 0.5	0.0 - 2.0	Small	a	0.0 - 0.3	Small
B	0.5 - 1.0	1.6 - 3.2	Moderate	b	0.3 - 0.5	Moderate
C	1.0 - 2.0	2.5 - 5.1	Heavy	c	0.5 - 1.0	Heavy
D	2.0 - 3.0	4.0 - 6.7	High	d	1.0 - 1.5	High
E	>3.0	5.3 - 18.0	Extreme	e	>1.5	Extreme

2.5. Decay tests

Free decay tests were carried out in surge, heave and pitch to estimate the damping ratios and natural periods of these free motions. The tests were started by giving the model an initial perturbation from equilibrium in the considered mode of motion, trying to minimize the coupling with other modes. From the free decays, the natural period of surge, heave and pitch are $T_{n,1} = 22.4$ s (116.4 s full-scale), $T_{n,3} = 2.12$ s (11 s full-scale), $T_{n,5} = 2.76$ s (14.36 s full-scale), respectively. The free surface inside the tank can be approximated as horizontal at these frequencies and surge and pitch can as a first approximation be

considered as uncoupled. Because it takes a long transient phase with given forcing frequency to develop steady-state interior waves (sloshing), these tests do not provide information about coupled natural period between surge, pitch and sloshing to be discussed below.

2.6. Resonance conditions for internal sloshing

In order to analyze the effects of sloshing phenomena inside the cage, we need to identify the occurrence and features of internal-water resonance and, therefore, the sloshing natural frequencies and modes. Natural modes are nontrivial solutions to the linear boundary-value problem for the water in the partially-filled cage without external cage excitation. According to Faltinsen and Timokha (2009), the velocity potential of liquid motion inside an upright circular cylindrical tank can be expressed in a cylindrical coordinate system $Or\theta z$ as

$$\varphi_{m,n}(r,\theta,z) = J_m(k_{m,n}r)\frac{\cosh\left[k_{m,n}(z+h_t)\right]}{\cosh\left(k_{m,n}h_t\right)}\begin{cases}\cos m\theta\\ \sin m\theta\end{cases} \tag{2}$$

where J_m is the Bessel function of the first kind of order m and h_t is the tank water depth. Furthermore, θ is defined in the right of Figure 1. $k_{m,n} = l_{m,n}/R_t$ with R_t the tank radius and $l_{m,n}$ the non-dimensional roots of the equation $J_m^{'}(l_{m,n}) = 0$ (symbol prime indicates derivative of the function) and $m = 0, 1, 2, ...,$ $n = 1, 2, 3....$ Both $\cos m\theta$ and $\sin m\theta$ modes can be excited. Given $k_{m,n}$, the natural periods $T_{m,n}$ corresponding to the different sloshing modes can be determined as

$$T_{m,n} = 2\pi/\sqrt{gk_{m,n}\tanh\left(k_{m,n}h_t\right)} \tag{3}$$

The surface wave patterns of the normal modes can be found as $f_{m,n}(r,\theta) = \varphi_{m,n}(r,\theta,0)$ and the sloshing mode shapes for $m = 0, 1, 2, 3$ and $n = 1, 2$, eight modes, are presented in Figure 4.

3. Signal processing

In this section, we will first introduce the approach to extract rigid body motions and radial elastic deformations from the measured translatory displacements of eight markers installed at the freeboard of the cage. Then, the procedure to identify excitation of the sloshing modes from the internal eight wave probes is explained. In regular waves, steady-state responses are of interest and the method to estimate the steady-state amplitude and phase from the measured time-series is also illustrated. In the last part, a brief explanation is given concerning the evaluation of transfer functions from the white-noise tests.

3.1. Motion measurement

As mentioned in Section 2.3, two approaches were implemented to capture the motions of the cage, i.e., using eight markers along the cage wall and using a three-markers system. The three-markers system can be used to track the 6 DOF linear rigid body motions for cases with negligible cage deformations. While by manipulating the translatory motions of eight markers, we can obtain both the rigid body motions and radial elastic deformations. Detailed explanation of the approach is given below.

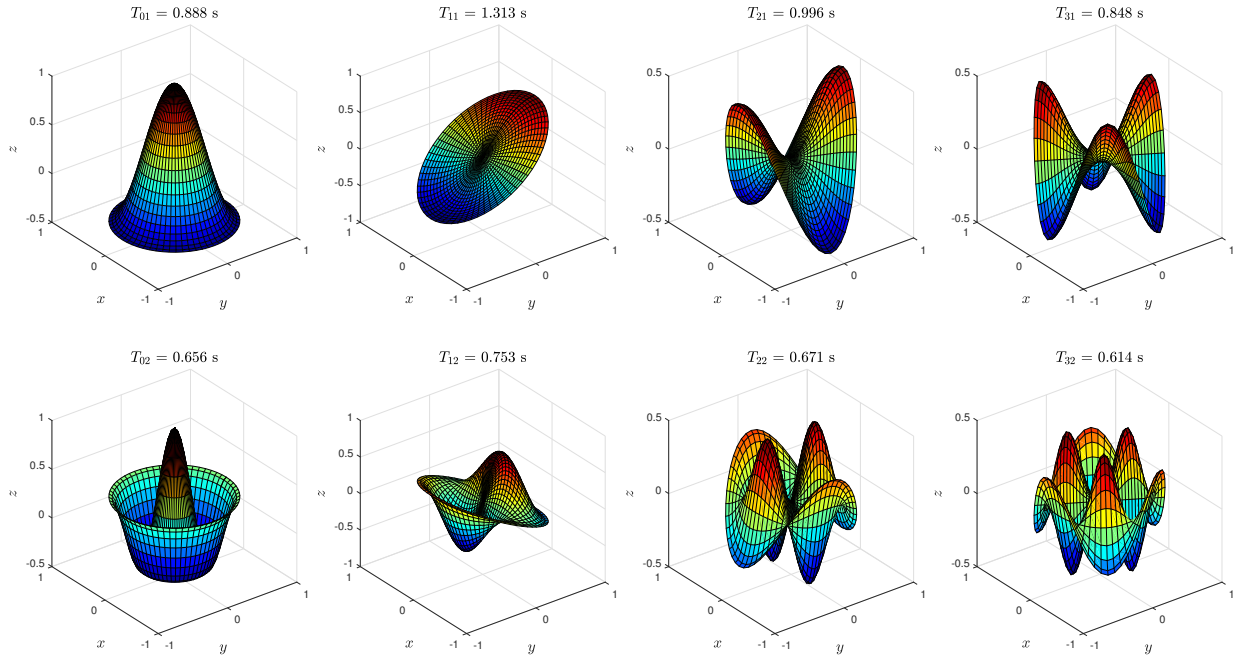

Figure 4: Surface wave pattern of sloshing modes ($\cos m\theta$, $m = 0, 1, 2, 3$, $n = 1, 2$) and corresponding natural periods $T_{m,n}$ in a vertical circular tank with radius $R_t = 0.745$ m and water depth $h_t = 0.73$ m.

According to linear theory, the translatory motions $\vec{s}_i$ of the i_{th} marker can be related to the body motions of the cage model as

$$\vec{s} = \vec{\eta}_{1-3} + \vec{\eta}_{4-6} \times \vec{r} + d\vec{r} \tag{4}$$

where $\vec{\eta}_{1-3}$ and $\vec{\eta}_{4-6}$ are the three dimensional vectors of translatory and rotational rigid-body modes of motion, respectively, while $\vec{r}$ is the position vector of the marker relative to the origin when at rest. The additional term $d\vec{r}$ is included to account for possible deformations of the cage. For the markers installed along the perimeter of the cage model with a given elevation Z, we will also operate with a cylindrical coordinate system $Or\theta z$ where $x = r\cos\theta, y = r\sin\theta, z = Z$. Equation 4 can be further expressed as

$$\begin{aligned}
\vec{s} &= s_1\vec{i} + s_2\vec{j} + s_3\vec{k} \\
&= (\eta_1 + z\eta_5 - y\eta_6)\,\vec{i} + (\eta_2 - z\eta_4 + x\eta_6)\,\vec{j} + (\eta_3 + y\eta_4 - x\eta_5)\,\vec{k} + d\vec{r} \\
&= (\eta_1 + Z\eta_5 - r\sin\theta\eta_6)\,\vec{i} + (\eta_2 - Z\eta_4 + r\cos\theta\eta_6)\,\vec{j} + (\eta_3 + r\sin\theta\eta_4 - r\cos\theta\eta_5)\,\vec{k} + d\vec{r}
\end{aligned} \tag{5}$$

To account for the deformation in the radial direction, at a given vertical position Z and radial distance $r = R$, alternatively, we can express the radial displacements as the following Fourier series in θ

$$\begin{aligned}
\eta_r(Z,t) &= \vec{s}\cdot\vec{n} \\
&= \sum_{m=0}^{\infty}\eta_{r,1,m}\cos m\theta + \sum_{m=1}^{\infty}\eta_{r,2,m}\sin m\theta
\end{aligned} \tag{6}$$

where $\vec{n} = (\cos\theta, \sin\theta, 0)$ and t is time. This second approach will be pursued in the following. In Equation 6, $\eta_{r,1,1}\cos\theta$ and $\eta_{r,2,1}\sin\theta$ are local normal component due to rigid-body surge and sway at level Z,

respectively. This can be expressed as $(\eta_1 + Z\eta_5)\cos\theta$ and $(\eta_2 - Z\eta_4)\sin\theta$, respectively. This leads to $\eta_{r,1,1}$ $= \eta_1 + Z\eta_5$ and $\eta_{r,2,1} = \eta_2 - Z\eta_4$. The contributions $\eta_{r,1,2}\cos 2\theta$ and $\eta_{r,2,2}\sin 2\theta$ are radial elastic ovalizing modes at level Z, as illustrated in Figure 5. Actually, the displacements in vertical direction along the cage can also be expressed as a Fourier series, similar as done in radial direction but the deformations in vertical direction are expected to be small. Therefore, to reduce complexity, we just consider rigid body motions and the vertical translatory motion is expressed as

$$\begin{aligned} \eta_z(Z,t) &= s_3 \\ &= \eta_3 + R\sin\theta\eta_4 - R\cos\theta\eta_5 \end{aligned} \tag{7}$$

We will first show the procedure to obtain η_3 and η_5. Equation 7 is projected along $\cos n\theta$. It means that both sides are multiplied by $\cos(n\theta)$, n=0,1,2,etc. Then, it is integrated in θ between 0 and 2π. This gives

$$\int_0^{2\pi} s_3 \cos n\theta d\theta = \int_0^{2\pi} [(\eta_3 + R\sin\theta\eta_4 - R\cos\theta\eta_5)\cos n\theta d\theta \tag{8}$$

s_3 is translatory motion in z direction and is a function of θ. It can be obtained by implementing cubic spline interpolation in θ from the measured vertical displacements of the eight markers. Using the property of orthogonal functions, the right side of the Equation 8 equals $2\pi\eta_3$ when $n = 0$; if $n = 1$, the value becomes $-\pi R\eta_5$. Similarly, projecting Equation 6 along $\cos(n\theta)$, n=0,1,2,etc, we can estimate coefficients $\eta_{r,1,m}$ for $\cos m\theta$ modes. Known $\eta_{r,1,1}$ and η_5, the rigid-body surge motion can be readily obtained. The same procedure is followed to obtain the $\sin m\theta$-related terms.

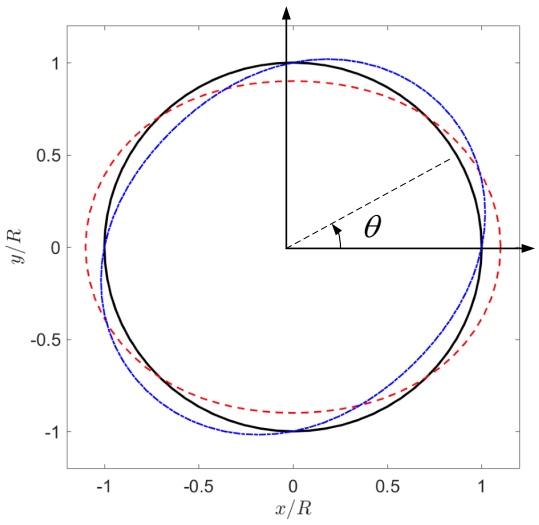

Figure 5: Illustration of the radial ovalizing modes. Black solid line: initial radial shape as a circle with radius R. Red dashed line: shape with radial deformation $0.1R \cdot \cos 2\theta$. Blue dash-dotted line: shape with radial deformation $0.1R \cdot \sin 2\theta$.

In regular waves, the linear steady state responses oscillating with incident wave frequency ω are of

interest. For instance, the steady state radial displacements are expressed as

$$\eta_{r,s}(Z,t) = \sum_{m=0}^{\infty} \eta_{ra,1,m} \cos(\omega t - \varepsilon_{ra,1,m}) \cos m\theta + \sum_{m=0}^{\infty} \eta_{ra,2,m} \cos(\omega t - \varepsilon_{ra,2,m}) \sin m\theta \tag{9}$$

Here $\eta_{r,s}$ is the linear steady state part of η_r. $\eta_{ra,j,m}$ and $\varepsilon_{ra,j,m}$, with $j = 1, 2$ are the corresponding amplitude and phase of $\cos m\theta$ and $\sin m\theta$ contributions, respectively. The phases are relative to the incident waves, which are described by

$$\zeta = \zeta_a \cos(\omega t + kx) \tag{10}$$

where ζ_a is the incident wave amplitude and k is the wave number. For all examined tests, k satisfies the deep-water dispersion relationship, i.e. $k = \omega^2/g$.

3.2. Internal wave elevation

The wave elevations are measured relative to the tank-fixed coordinate system. To relate the internal wave with the natural sloshing modes, Fourier modes in θ for the internal waves are extracted, based on the measurements from eight internal wave probes RW1-8. The free surface level inside the container at a given radial distance $r = 0.95R$ is expressed as

$$\zeta_{int}(t) = \sum_{m=0}^{\infty} \zeta_{1,m} \cos m\theta + \sum_{m=1}^{\infty} \zeta_{2,m} \sin m\theta \tag{11}$$

Employing the same strategy as done in Section 3.1, we can have the coefficients $\zeta_{1,m}$ and $\zeta_{2,m}$ for $\cos m\theta$ and $\sin m\theta$ modes, respectively. In regular waves, the corresponding steady-state linear free surface level is expressed as

$$\zeta_{int,s}(t) = \sum_{m=0}^{\infty} \zeta_{a,1,m} \cos(\omega t - \varepsilon_{a,1,m}) \cos m\theta + \sum_{m=1}^{\infty} \zeta_{a,2,m} \cos(\omega t - \varepsilon_{a,2,m}) \sin m\theta \tag{12}$$

Here $\zeta_{int,s}$ is the linear steady state part of ζ_{int}. $\zeta_{a,j,m}$ and $\varepsilon_{a,j,m}$, with $j = 1, 2$ are the corresponding amplitude and phase of $\cos m\theta$ and $\sin m\theta$ modes, respectively.

3.3. Transfer function in regular waves

The incident waves can be considered as deep-water waves. For illustration, a typical time history of surge motion in regular wave is shown in the left plot of Figure 6. The considered incident-wave period and height are, respectively, $T = 1.02$ s and $H = 0.027$ m. There is clearly a beating component with period of about 22.4 s. This is the natural surge period of the system consisting of mooring lines and the cage. Longer time is needed to damp out this slowly varying component due to the small associated damping. To estimate the steady-state response and phase, a time interval is extracted where the system is considered to have reached steady state. The start time of this window is evaluated as $t_s = t_p + t_{ramp}$. Here $t_p = L_d/C_p$ is the time needed by the wave front for the consided regular wave to travel from the wavemaker to the model center position, by asssuming linear wave theory. L_d is the distance between the wavemaker and the model

and C_p is the wave group velocity. $t_{ramp} = 35T$ is used to remove the start-up transient stage, as illustrated in the right of Figure 6. The end time is chosen as $0.95t_{tot}$ with t_{tot} the length of the measured time series. Two strategies are adopted to evaluate the corresponding amplitude and phase of the response variable of interest. The first is applying the Fast Fourier transform (FFT) for the considered steady-state interval. Then the amplitude and phase for the first harmonic component can be easily obtained. The time series is tapered at both ends by means of a Bingham window (Harris, 1978) to reduce end-effects of the extracted time interval. The main shortcoming of this method is the unavailability of error bar of the amplitude, which may serve as an indication of whether steady state is achieved. Alternatively, we attempt to extract the response component oscillating with ω using band-pass filtering. Only signal with frequency equal to ω is kept. A Gaussian mask (Hansen, 2014) is multiplied to the signal frequency spectrum obtained by Fourier transform (FFT). The derived time history and the related envelope are shown in the right plot of Figure 6. Similar as in the first method, a steady-state time window is chosen and the Hilbert transform (Oppenheim et al., 2001) is used for calculating instantaneous properties of the resulting time series. Eventually, the mean values, representing the amplitude of the measurements, and the standard deviations of the envelope curves are obtained. The phase relative to the incident wave can be easily obtained by calculating the time offset δt of zero up-crossing between the two time series (the response and the incident-wave signals) and estimated as $2\pi\delta t/T$. The latter method is used for further analysis of transfer functions of the measured variables.

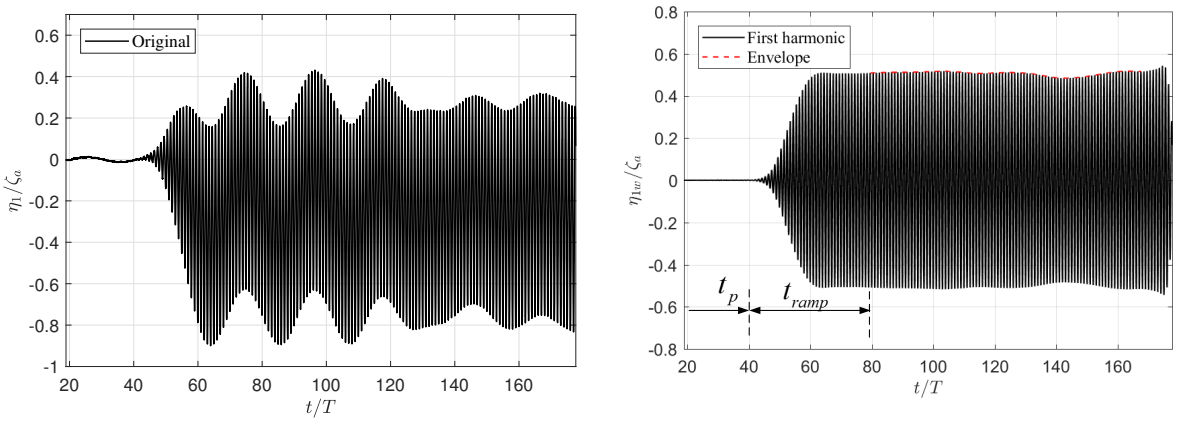

Figure 6: Left: example of time history of the surge motion of the cage for $T = 1.02$ s and $H = 0.027$ m. Right: time history of the first harmonic component of the signal shown in the left.

3.4. Transfer function in irregular waves

For white noise tests, transfer functions can be estimated in two ways, using power spectral density (PSD) and cross power spectral density (CPSD) of the incident wave and the measured variables (Bendat and Piersol, 2011). To evaluate the relevant spectra, the signal is chopped into time windows. In each of them a Fourier transform is applied to determine its frequency components. The predictions made in these

time windows are then averaged to produce the estimated spectra (Welch, 1967). As an example, the transfer function of surge motion is given as

$$|H_{\eta_1\eta_1}| = \sqrt{S_{\eta_1\eta_1}/S_{\zeta\zeta}} \quad \text{or}$$
$$H_{\eta_1\zeta} = S_{\eta_1\zeta}/S_{\zeta\zeta} \tag{13}$$

where $|H_{\eta_1\eta_1}|$ is the response amplitude operator for surge from PSD, $S_{\eta_1\eta_1}$ is the power spectrum of surge motion and $S_{\zeta\zeta}$ the power spectrum of incident wave; $H_{\eta_1\zeta}$ is the complex response operator for surge from CPSD, including both amplitude and phase information, $S_{\eta_1\zeta}$ is the cross power spectrum between surge motion and incident wave and is a complex variable. A comparison of the response amplitude operator of surge motion from the two methods is presented in Figure 7 versus incident wavelength-to-diameter ratio λ/D. The two methods yield similar results for shorter waves where the system is expected to behave more like a linear system. Larger difference is observed for longer waves, i.e. involving periods larger than the relevant sloshing natural periods. This suggests more pronounced nonlinear effects in surge as a consequence of its coupling with pitch. In fact, longer waves can induce stronger nonlinearities in pitch due to possible in and out of water on the floating collar. This explanation is supported by later Figure 13, where the linear potential-flow solver WAMIT provides a poor prediction for pitch in longer waves. Since both the amplitude and phase information are of interest, the method based on CPSD will be further adopted to calculate the transfer functions for the measured variables.

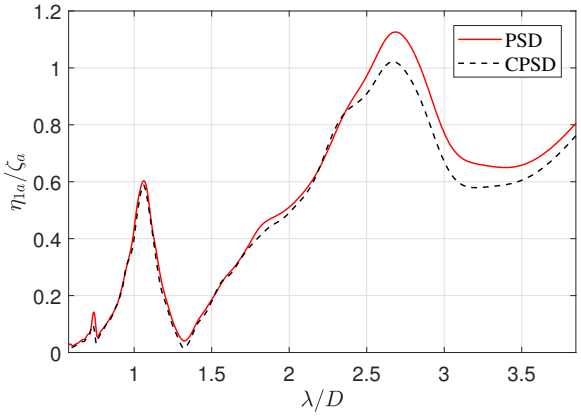

Figure 7: Response amplitude operator of surge motion (transfer function) η_{1a}/ζ_a versus relative wavelength λ/D obtained from a truncated white-noise test with significant wave height $H_s = 0.037$ m. PSD = power spectral density. CPSD = cross power spectral density.

4. Experimental results and discussions

In this section, we show and discuss selected results from the model tests for the closed cage. Firstly, the experimental accuracy in the generation of prescribed (regular and white noise) waves is assessed. Then transfer functions of the measured variables are shown. Finally, the mean wave drift forces acting on the cage

are examined. Results from the linear potential flow solver WAMIT (Lee, 1995) are also provided, assuming a rigid structure. The sloshing part was verified by comparing with analytical expressions for surge and pitch added mass presented by Faltinsen and Timokha (2009). Hydroelasticity was studied by combining WAMIT with LS-DYNA (Hallquist, 2007).

4.1. Incident waves

In order to quantify the experimental reliability in generating the prescribed waves, preliminary wave-propagation tests were performed with no model present in the wave basin. An example of incident regular-wave time history is given in the left plot of Figure 8 with prescribed period and height, respectively, $T = 1.02$ s and $H = 0.027$ m. To estimate the actual incident wave height, the strategy described in Section 3.3 is implemented and only the first harmonic component is considered. The averaged wave height becomes 0.0246 m, about 9% smaller than the precribed value. A more detailed comparison between the experimental and theoretical wave heights is shown in the right of Figure 8. The generated incident waves at the model location were found to be in good agreement with the prescribed regular wave parameters for shorter waves, but larger deviations were observed for longer waves.

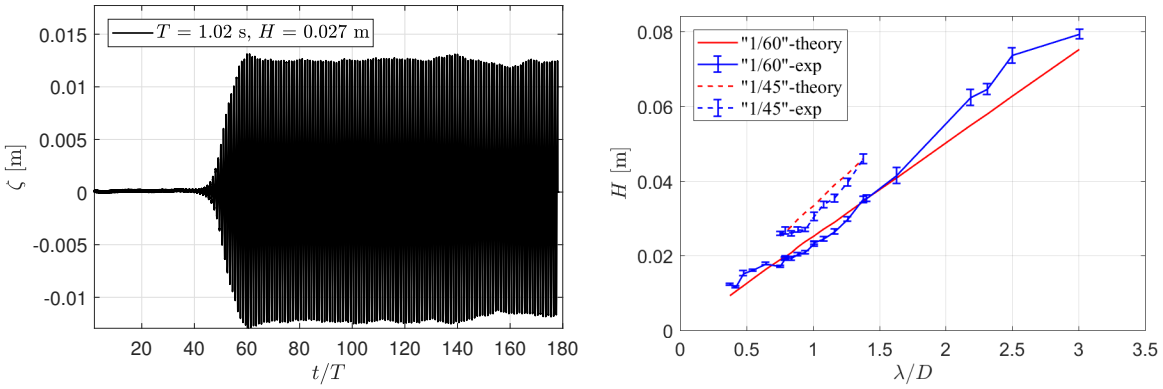

Figure 8: Left: example of incident regular-wave time history for prescribed period $T = 1.02$ s and height $H = 0.027$ m. Right: comparison of the regular wave heights from the experiments (mean values and standard deviation) and from the linear wave theory versus λ/D. Two wave steepnesses $H/\lambda = 1/60$ and $1/45$ are considered.

Tests with incident waves generated according to the truncated white noise spectrum with and without the model were also performed. An example of incident white-noise wave time history is provided in the left of Figure 9. The prescribed significant wave height is $H_s = 0.037$ m and the frequency region with energy is between 0.208Hz and 1.732Hz, the corresponding λ/D changes between 0.346 and 15.42. Theoretically, the waves should have equal energy within the prescribed frequency region, as shown by the red dashed line in the right of the plot of the figure.

The actual spectral density varies but with mean value close to the theoretical value. The actual measured incident-wave parameters will be used when evaluating the transfer functions. However, for convenience the prescribed incident-wave parameters will be used in the figures captions and in the main text.

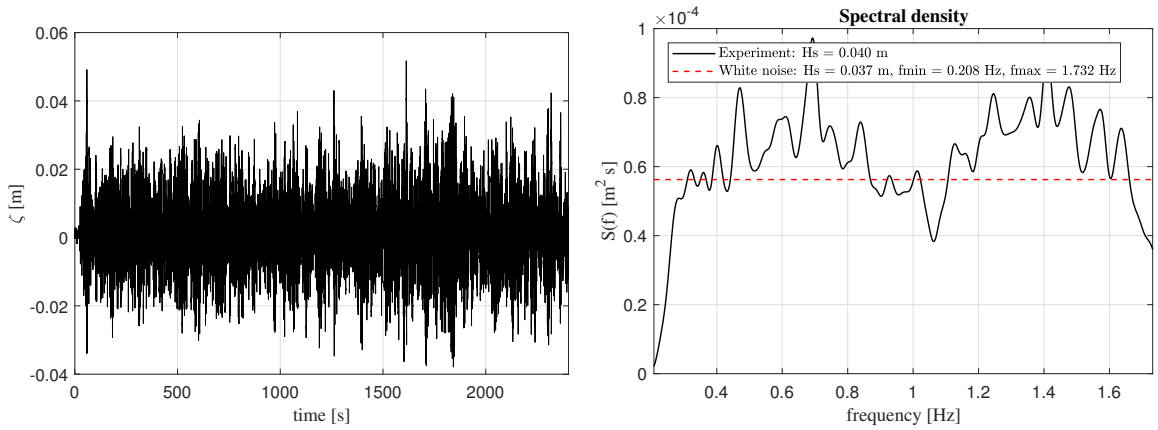

Figure 9: Left: time history of incident wave from truncated white noise spectrum with prescribed significant wave height H_s = 0.037 m. Right: comparison of wave spectral density from the experiment with the theoretically desired value.

4.2. Transfer function of rigid cage motions

As mentioned in Section 2.3, the motions of the cage were measured with two methods, either using the eight markers along the cage wall or obtained directly from the three-markers system. The former can provide both rigid motions and radial elastic deformations of the cage, while the latter can provide 6 DOF rigid body motions directly and is only applicable for bodies acting as fully rigid. Figure 10 shows the time histories of the surge, heave and pitch motions obtained from the two methods for the case with T = 2.5 s, H= 0.163 m and H/λ = 1/60, corresponding to λ/D = 6.5. The cage is expected to have negligible deformations for the examined case as it will tend to follow the waves, so the three-markers system could provide reliable rigid body motions. The figure confirms that the two measurement techniques give consistent results, showing the reliability of extracting the rigid and elastic body motions from the eight markers.

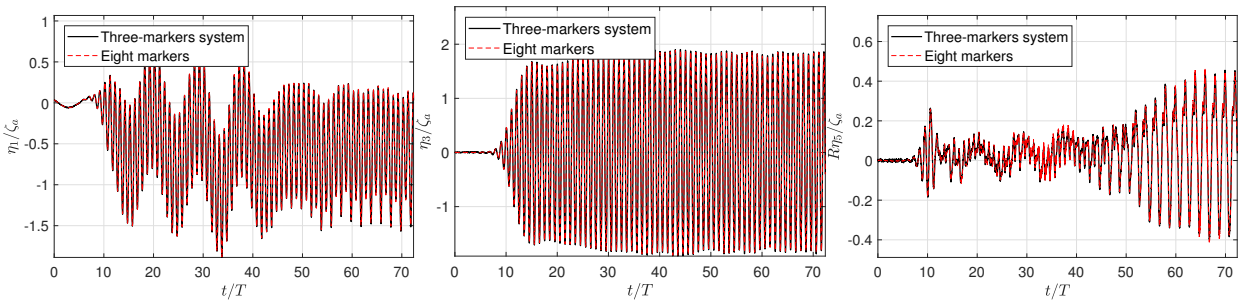

Figure 10: Time histories of the surge (left), heave (middle) and pitch (right) motions of the closed cage. Solid black line: from the three-markers system. Dashed red line: from the distributed eight markers at the freeboard. T = 2.5 s, H = 0.163 m and λ/D = 6.5. $R = D/2$ is the outer radius of the closed cage.

Things change when the wavelength is not large compared to the cage diameter. This is shown by the case with T = 1.02 s, H= 0.027 m and H/λ = 1/60, corresponding to λ/D = 1.08. The time histories of the rigid body motions are shown in Figure 11. The two measurements provide similar results at the initial stage, but after about 70 periods, larger difference is observed when the waves inside the cage become high

in time and large ovalizing structural modes are excited. The main reason for the difference is that the three-markers system in principle cannot be applied for tests with non-negligible body deformations as the rigid body motions can not be separated from the elastic deformations. A more detailed comparison of the rigid body motions from the two measurements for different wave periods is shown in Figure 12. From the figure, the two approaches provide consistent results for surge and heave motions in long waves ($\lambda/D > 1.6$). Larger differences are observed for all the three examined motions in short waves ($\lambda/D < 1.5$), especially for wave periods close to the sloshing natural period T_{21} where the cage experiences large ovalization deformations. The rigid body motions from the eight markers will be used for further analysis.

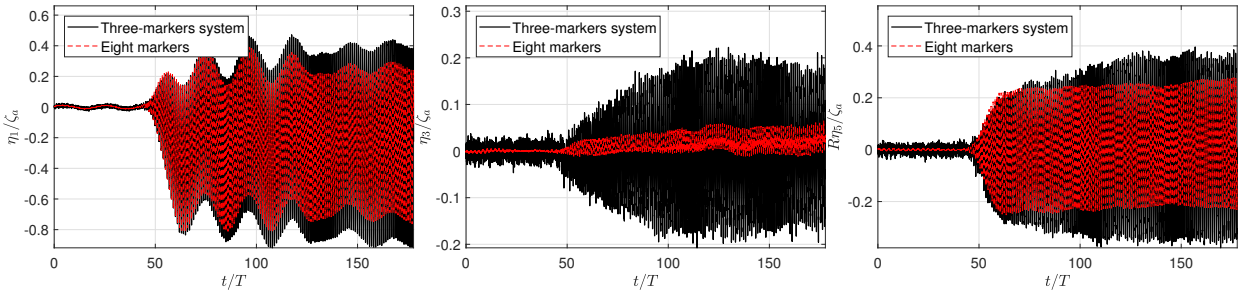

Figure 11: Same as in Figure 10, but for $T = 1.02$ s, $H = 0.027$ m and $\lambda/D = 1.08$.

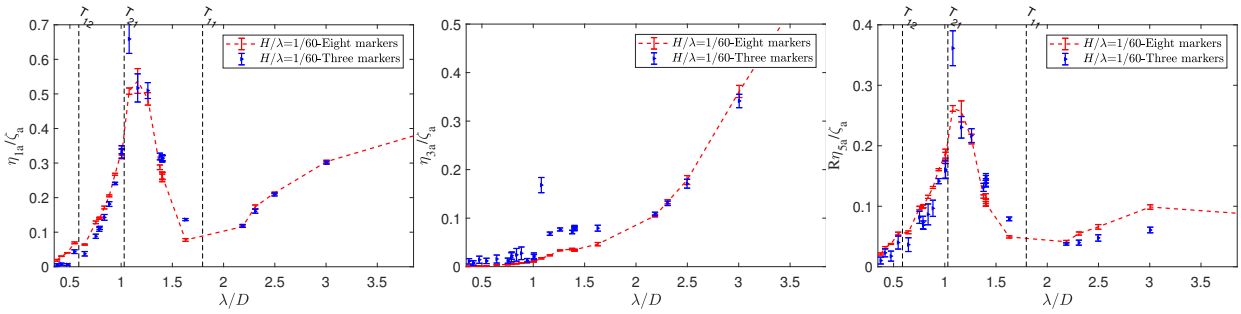

Figure 12: Comparison of transfer functions of surge, heave and pitch from the two measurements in regular waves versus nondimensional wave length λ/D. Wave steepness $H/\lambda = 1/60$. T_{ij} = natural sloshing periods.

Figures 13 shows the comparisons for surge, heave and pitch in a frequency range of primary importance for local wind generated waves. Experimental data from both regular waves and the two white noise tests are given. Results from the linear potential-flow solver WAMIT are also provided. Motion amplitudes from regular waves in general agree nicely with those from the white noise tests, especially when the latter is with smaller significant wave height, i.e., $H_s = 1/27$ m. The wave periods examined are far from the relevant rigid-body natural periods without coupling to sloshing. Results from the two white noise tests match well for shorter waves ($\lambda/D < 1.5$), but larger differences are observed for longer waves where the system is characterized by stronger nonlinearities, as discussed later. These may involve in general both potential-flow and viscous-flow effects, with the latter connected with flow separation. However, calculations with an equivalent linearized damping corresponding to 10% of the critical damping were also performed by WAMIT

(not shown here) to check the effect of viscous damping and small influence was observed for λ/D <4. As a note, the "longer waves" examined here correspond to periods still far from the natural pitch period.

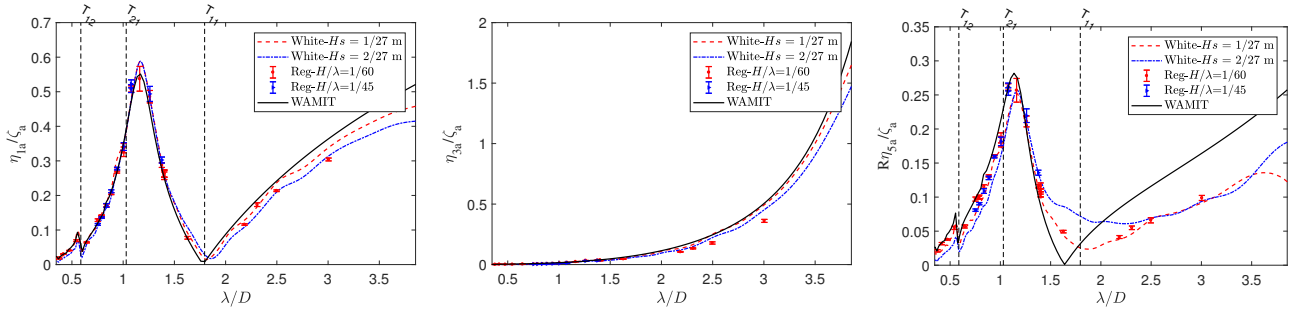

Figure 13: Transfer functions of surge, heave and pitch versus relative wavelength λ/D. λ is the wave length and $D = 2R$ is the cylinder diameter. ζ_a is incident wave amplitude. Black solid lines are from WAMIT calculations. Other data are based on experiments in either regular or truncated white noise waves. T_{ij} = natural sloshing periods.

Important sloshing natural periods $T_{11} = 1.313s$, $T_{21} = 0.996s$ and $T_{12} = 0.753s$ in model scale are denoted with vertical dashed lines in the figure. Surface wave pattern of the three sloshing modes are exemplified in Figure 4. We should note that nearly zero surge is happening at $\lambda/D = 1.794$ (corresponding to $T = T_{11}$), which is consistent with linear sloshing theory when surge is uncoupled from pitch. A coupled sloshing-surge-pitch natural period occurs according to linear theory at $\lambda/D = 1.162$, where we see a clear peak in theoretical and experimental results of surge and pitch. It should be pointed out that $\lambda/D = 1.03$ corresponds to $T = T_{21}$. The latter fact and closeness to the peak value at $\lambda/D = 1.162$ together with the fact that violent sloshing occurs must not be misinterpreted as sloshing resonance associated with T_{21}. Resonant oscillations associated with T_{21} cannot be excited according to linear theory for a rigid structure. There is overall a good comparison between WAMIT and the experimental surge, heave and pitch transfer functions. However, we note some differences for pitch for λ/D >1.4. One reason can be large relative vertical motions at the floating collar causing nonlinearities of more importance for pitch than for surge and heave. This can be directly seen by examining the restoring coefficients and the Froude-Kriloff excitation loads, which partly can be associated with the relative vertical wave elevation at the floater.

The measured relative wave elevation outside the cage is shown in Figure 14 for the regular wave cases with steepness $H/\lambda = 1/60$. Peaks and absolute values of troughs of the wave elevations from the three wave probes RW9, RW11 and RW13 (defined in Figure 1) are included. The values are made nondimensional by the cross-sectional radius of the floating collar r_f. The figure shows that the relative wave height in the front wave probe RW9 is apparently larger than in the side (RW11) and back (RW13) probes. For cases with $\lambda/D > 1.4$, the nondimensional relative wave amplitude is larger than 1, implying that the front part of the floating collar will go in and out of the water. This coincides with the region where WAMIT provides poor prediction of the pitch motion. The large relative vertical motions suggest that flow separations occur. We can make the analogy of ambient one-dimensional oscillating flow past a 2D circular cylinder in infinite fluid and introduce the Keulegan-Carpenter number $\mathrm{KC} = \pi\zeta_{\mathrm{rel,a}}/\mathrm{r_f}$. The flow separates from the analogue

cylinder when KC>∼2.

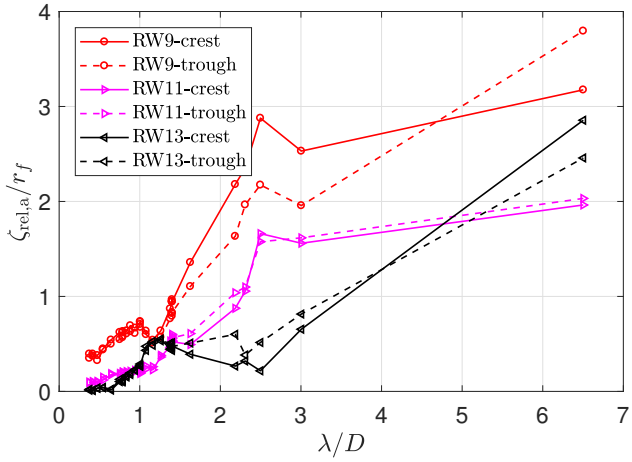

Figure 14: Non-dimensional relative wave amplitude $\zeta_{\mathrm{rel,a}}/r_f$ from the three outside wave probes RW9, RW11 and RW13 (see Table 2). This is expressed both as crest value and as absolute value of the trough. r_f is the cross-sectional radius of the floating collar. Presented versus relative wave length λ/D for $H/\lambda = 1/60$.

Comparisons of the phase of the motions from the experiments and from WAMIT calculations are presented in Figure 15. The values from the regular wave tests and white noise tests are consistent, which demonstrates the feasibility of performing white noise tests to obtain the transfer functions. Also, reasonable good agreement between the numerical and experimental results is obtained. This is consistent with the discussion in Section 1 concerning the fact that the sloshing response can be mild if the coupled natural frequency $\omega_{\mathrm{coupl},1}$ is not close to the natural sloshing frequency ω_1. In fact in this case $\omega_{\mathrm{coupl},1}/\omega_1$=1.25 and a linear potential solver can provide reasonable predictions. One needs to point out that the results from the regular wave tests show a jump in the surge from value close to -180° to approximately 180° near λ/D=1 (see left of Figure 15). This is connected with the analysis used to estimate the phase angle defined between -180° and 180°. We could manually change the sign of the phase in order to avoid the jump but we preferred to leave the results as obtained from the analysis, in any case this does not affect the actual complex transfer function.

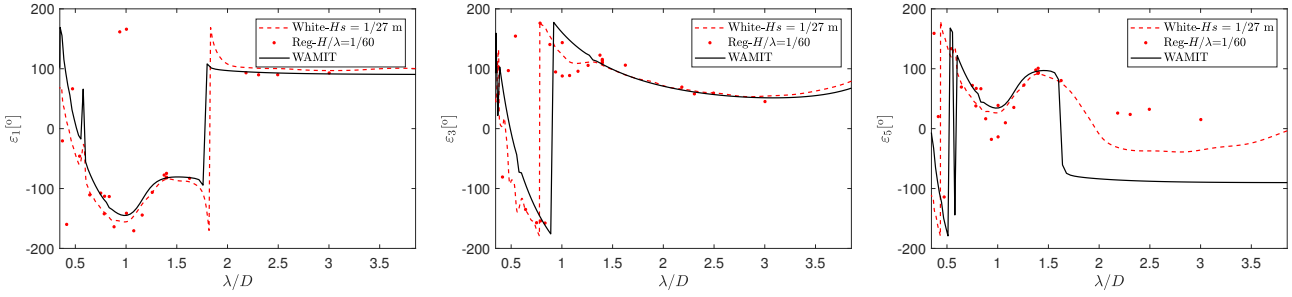

Figure 15: Same as in Figure 13, but for phase angles.

Response amplitude operators for $\lambda/D > 3.7$ are also presented to examine the behavior of the system

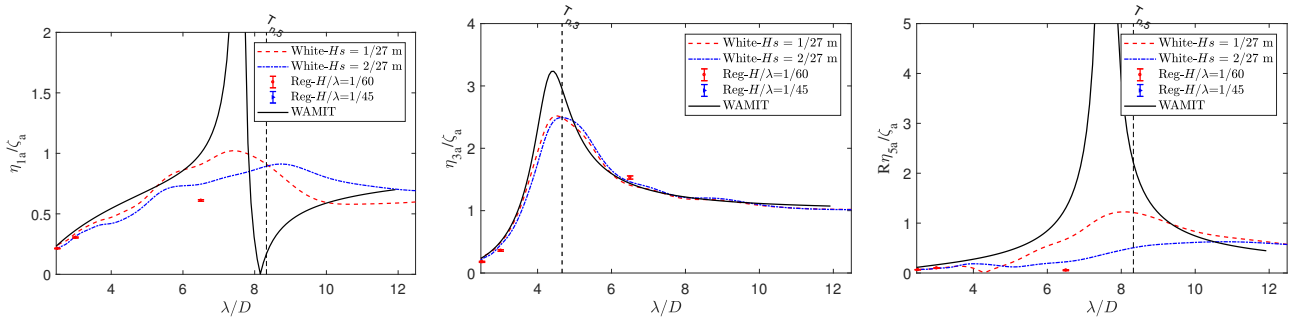

Figure 16: Same as in Figure 13, but for larger wave lengths. $T_{n,3}$ and $T_{n,5}$ are uncoupled natural periods in heave and pitch, respectively.

in long waves, see Figure 16. WAMIT predicts a coupled surge-pitch natural period corresponding to λ/D = 7.6. Since the wave-radiation damping is very small, large resonant values are predicted. The white-noise tests with lower wave amplitude indicate mild peaks in surge and pitch at slightly larger λ/D, while the tests at larger wave amplitude do not document clear peaks in this wavelength region. This suggests an importance of nonlinear, viscous and potential-flow, effects in the tests. Since these nonlinearities are not so important, for instance, for the heave restoring coefficient, WAMIT documents a reasonable agreement with experimental resonant heave values. To understand better the wave-body interaction close to the resonance zone, we can examine the corresponding regular-wave case. A regular wave test with T = 2.5 s, corresponding to λ/D = 6.5, was performed with H = 0.163 m and the time histories of motions are shown in Figure 10. The heave motion transfer function from regular wave test matches with the white-noise value but this is not the case for the surge and pitch, especially for the pitch. A so-called Mathieu-type instability occurred for the pitch motion for the regular-wave case due to in and out of water of the floating collar as a consequence of large heave motion and heave-pitch coupling, see snapshots shown in Figure 17. Mathieu-type of instability is well-known for parametric roll of ship (Ghamari et al., 2020) and for buoys (Haslum and Faltinsen, 1999). The pitch motion comprises two harmonic components, oscillating with T and $2T$, respectively. The corresponding time histories are shown in the left plot of Figure 18. The subharmonic $2T$ is the one connected with the pitch instability, becoming dominant as time goes on, and can not be predicted by linear potential theory.

The metacentric height GM = $\mathrm{C}_{55}/\rho \mathrm{g} \nabla$ with C_{55} given in Equation 1 is modified by a quasistatic formulation where the effect of heave and incident wave is accounted for. It means that $\rho g \int_{A_{W,f}} x^2 ds$ is modified by considering measured relative vertical elevations at the floating collar as presented in Figure 14. Furthermore, $\rho g \nabla z_b$ is modified by accounting for the relative vertical motions. The time history of GM is shown in the right of Figure 18. From the figure, we note that GM has a constant term $\overline{\mathrm{GM}}_{\mathrm{m}}$ plus a time-dependent term. The dominant component of the latter follows $\delta\overline{\mathrm{GM}} \cos(\omega_{\mathrm{GM}} t + \varepsilon_{\mathrm{GM}})$ with $\delta\overline{\mathrm{GM}}$, ω_{GM} and $\varepsilon_{\mathrm{GM}}$ the corresponding oscillation amplitude, frequency and phase, respectively. The pitch behavior can be explained by introducing Mathieu equation. The Mathieu equation follows by setting up the uncoupled

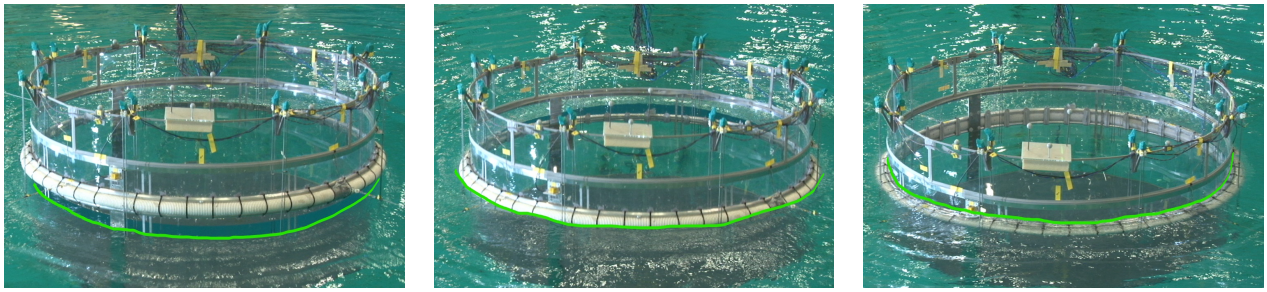

Figure 17: Snapshots of the cage model from the camera above the water surface for $T = 2.5$ s, $H = 0.163$ m and $\lambda/D = 6.5$. The local free-surface profiles are outlined by green lines.

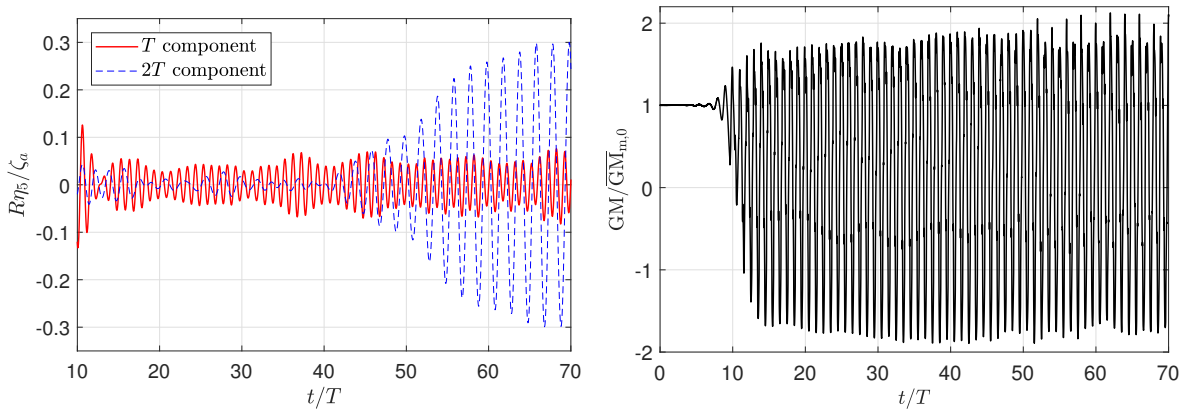

Figure 18: Left: time histories of the T and $2T$ components extracted from the pitch motion for the regular-wave case with $T = 2.5$ s, $H = 0.163$ m and $\lambda/D = 6.5$. Right: time history of the corresponding non-dimensional metacentric height GM. $\overline{\mathrm{GM}}_{\mathrm{m},0}$ is the inital metacentric height in calm water.

pitch equation with zero excitation and is given as

$$\left(I_{55}+A_{55}\right)\ddot{\eta}_5+\rho g\nabla\overline{\mathrm{GM}}_m\left[1+\frac{\delta\overline{\mathrm{GM}}}{\overline{\mathrm{GM}}_m}\cos\left(\omega_{\mathrm{GM}}t+\varepsilon_{\mathrm{GM}}\right)\right]\eta_5=0 \tag{14}$$

Here I_{55} and A_{55} are the inertia moment and added mass for the pitch motion, respectively. The undamped natural frequency for pitch is expressed as $\omega_{n,5}=\sqrt{\rho g\nabla\overline{\mathrm{GM}}_m/\left(I_{55}+A_{55}\right)}$. From Figure 18, the new mean metacentric height $\overline{\mathrm{GM}}_{\mathrm{m}}=0.32\cdot\overline{\mathrm{GM}}_{\mathrm{m},0}$ with $\overline{\mathrm{GM}}_{\mathrm{m},0}$ the inital metacentric height in calm water. This leads to the change of $\omega_{n,5}$ from 0.427 rad/s to 0.244 rad/s. The time-dependent term oscillates with frequency $\omega_{\mathrm{GM}}=\omega=0.483rad/s$ and amplitude $\delta\overline{\mathrm{GM}}=5.37\cdot\overline{\mathrm{GM}}_{\mathrm{m}}$. Figure 19 shows the stability diagram for Mathieu equation from Klotter (2013). For the examined case, $\omega_{n,5}/\omega=0.5$ and $\delta\overline{\mathrm{GM}}/\overline{\mathrm{GM}}_{\mathrm{m}}=5.37$, corresponding to the red circle in the figure. Because in our case $\xi\omega_n/\omega=0.0178$ with ξ as the damping ratio between pitch radiation damping and the critcal damping, the Mathieu instability will then be excited. Similar phenomenon was observed in an irregular wave test (not discussed in detail in the present paper) with peak wave period $T_p=1.924$ s and significant wave height $H_s=0.11$ m, corresponding in full scale to the extreme sea state defined in Table 3. The relevant power spectra for the incident wave, heave and pitch motions are shown in Figure 20. The peak pitch response occurs at wave period close to $2T_{n,3}$ instead of at the natural pitch period $T_{n,5}$ due to large resonant heave motion at $T_{n,3}$.

Since our focus is on wave conditions associated with local wind generated waves, more detailed discussions for the system in long waves and about the importance of accounting for system nonlinearity are left for future work.

High harmonic components of the rigid body motions from the regular waves tests are also analyzed and are generally moderate compared with the first harmonic value, i.e., less than 10%.

4.3. Transfer function of radial elastic deformations

As explained in Section 3.1, we can extract both rigid body motions and radial elastic deformations from the measurements of eight markers installed at the freeboard of the cage. Figure 21 presents the transfer functions of the ovalizing modes $\cos 2\theta$ and $\sin 2\theta$ of the fish cage at $z=0.35$ m from both the regular wave tests and white noise tests. The fact that the ovalizing mode $\sin 2\theta$ occurs is partly a consequence of structural asymmetry. The peak deformation occurs at $\lambda/D=1.078$ ($T=1.018$ s) for both modes, close to the corresponding sloshing natural period T_{21}=0.996 s. We should note that the value is different from the coupled sloshing-surge-pitch natural period and is a consequence of coupling between structural ovalizing modes and corresponding sloshing modes. Results from the regular wave tests are in general consistent with those from the white-noise tests, except near the resonant zone. The difference between the two white-noise tests at the resonant frequency indicates the occurrence of free-surface nonlinearities. Similar difference was observed between the results from the white-noise tests and irregular wave tests (not presented in the paper).

Time histories of the ovalization modes from the regular wave test at the resonant period are shown in Figure 22. Two extra elastic modes are included. The figure shows that the ovalizing modes dominate

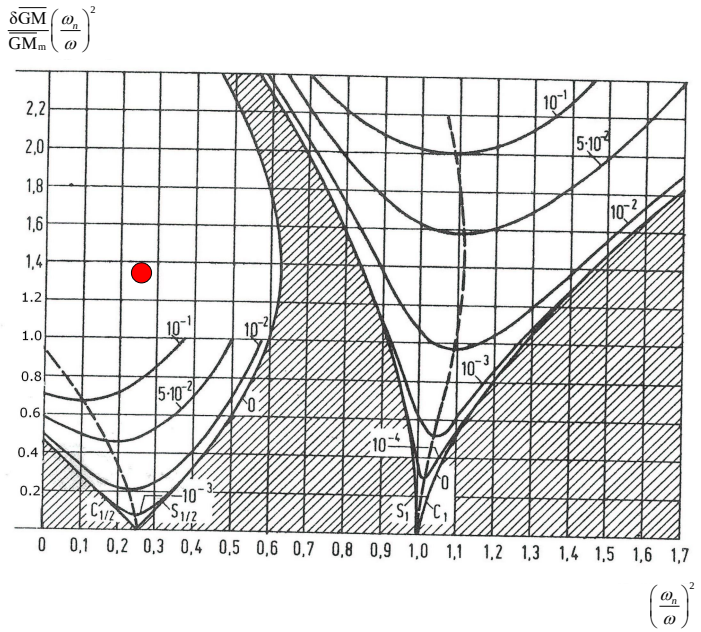

Figure 19: Stability diagram for the Mathieu equation applied to cage pitch motion without damping, adopted from Klotter (2013). There are also lines shown with values at $\xi\omega_n/\omega = 10^{-4}, 10^{-3}, 10^{-2}, 5\cdot10^{-2}$ and 10^{-1}, where ξ is the ratio between pitch damping and the critical damping. These lines are boundaries between stable and unstable domains. The labels for the x and y axes are slightly modified. The red circle corresponds to the examined case with $T = 2.5$ s, $H = 0.163$ m and $\lambda/D = 6.5$.

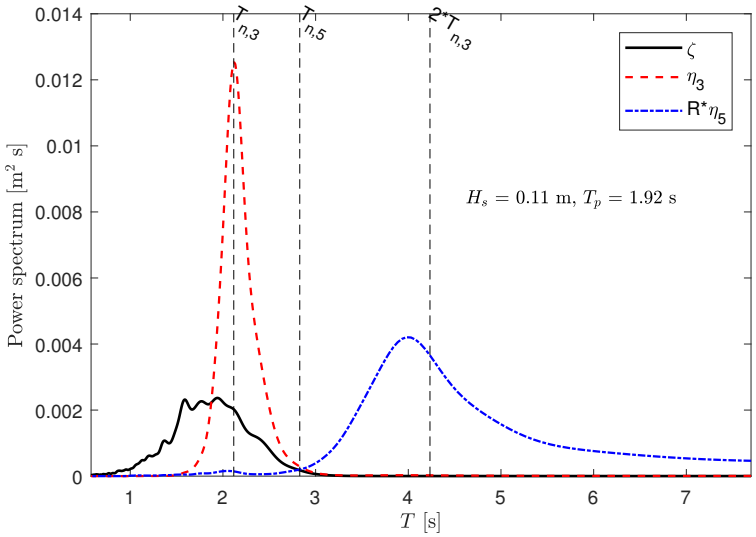

Figure 20: Power spectra for incident wave, heave and pitch motions from an irregular wave test with peak wave period $T_p = 1.924$ s and significant wave height $H_s = 0.11$ m ($T_p = 10$ s and $H_s = 3$ m full-scale). $T_{n,3}$ = natural heave period. $T_{n,5}$ = natural pitch period.

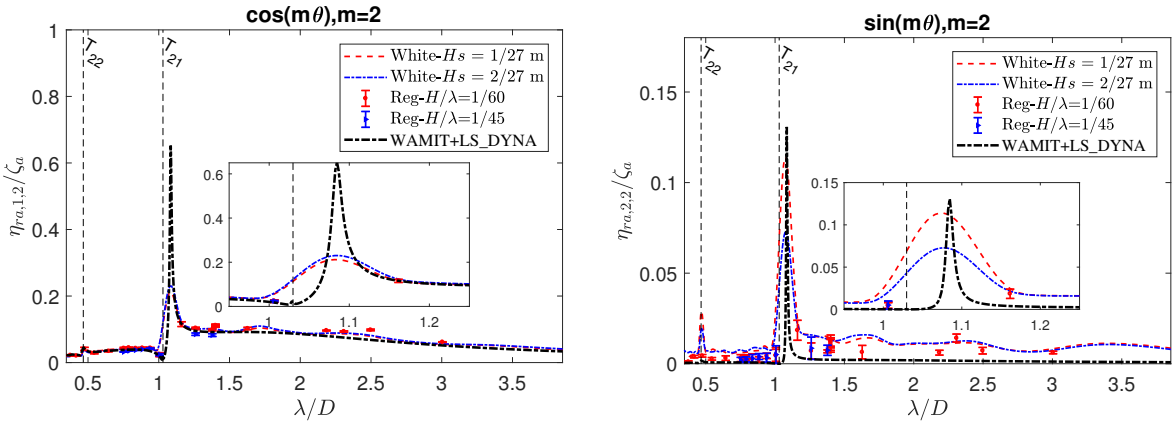

Figure 21: Transfer function of the radial deformation of the ovalizing modes $\cos(2\theta)$ and $\sin(2\theta)$ of the fish cage measured at the freeboard level versus nondimensional wave length λ/D. A zoomed view at the resonant zone is also provided. T_{21} and T_{22} = natural sloshing periods for ovalizing modes.

over other modes and due to small damping do not reach steady state within the time duration of the test. The build-up of the $\sin 2\theta$-mode is initially slower than for the $\cos 2\theta$-mode. Later on the values of the two ovalizing modes become similar in magnitude. One reason may be coupling with nonlinear sloshing and associated transfer of energy as detailed studied by Faltinsen and Timokha (2009) for prescribed horizontal motion of a rigid vertical tank near the highest sloshing period. Due to unrealistic large error bar associated, the corresponding regular-wave values are not presented in Figure 21. The fact that the $\sin 2\theta$-component is clearly smaller than the $\cos 2\theta$-component outside resonance is qualitatively consistent with the structural asymmetry introduced by the construction of the vertical cylinder and the cross-bar exterior to the tank bottom (see Figure 2). The transfer functions of other elastic modes are small, i.e., less than 2%, so are not presented here.

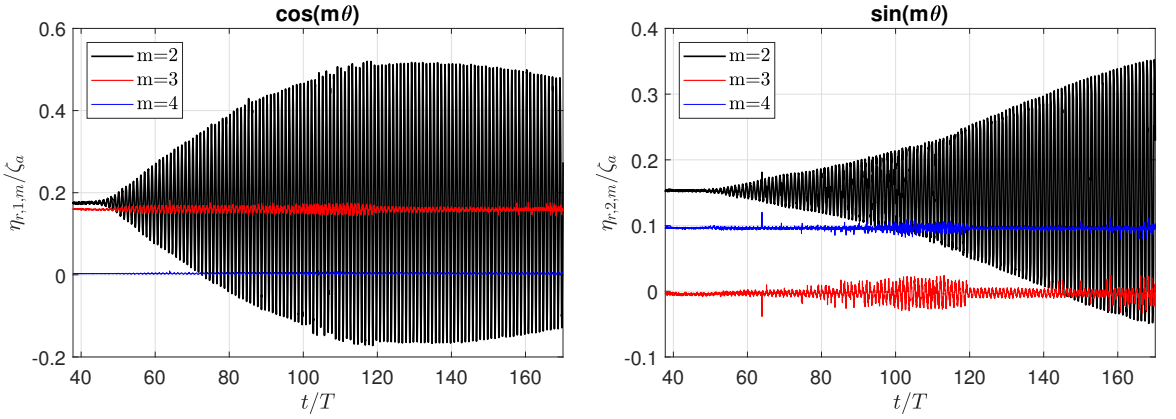

Figure 22: Measured time histories of radial deformation modes of the cage at $z = 0.35$ m. Only the first three elastic modes are included for $T = 1.02$ s, $H = 0.027$ m and $\lambda/D = 1.08$. Left: $\cos m\theta$ modes. Right: $\sin m\theta$ modes.

The ratio between the wet and dry natural periods of the ovalizing modes is 9. A major reason is the

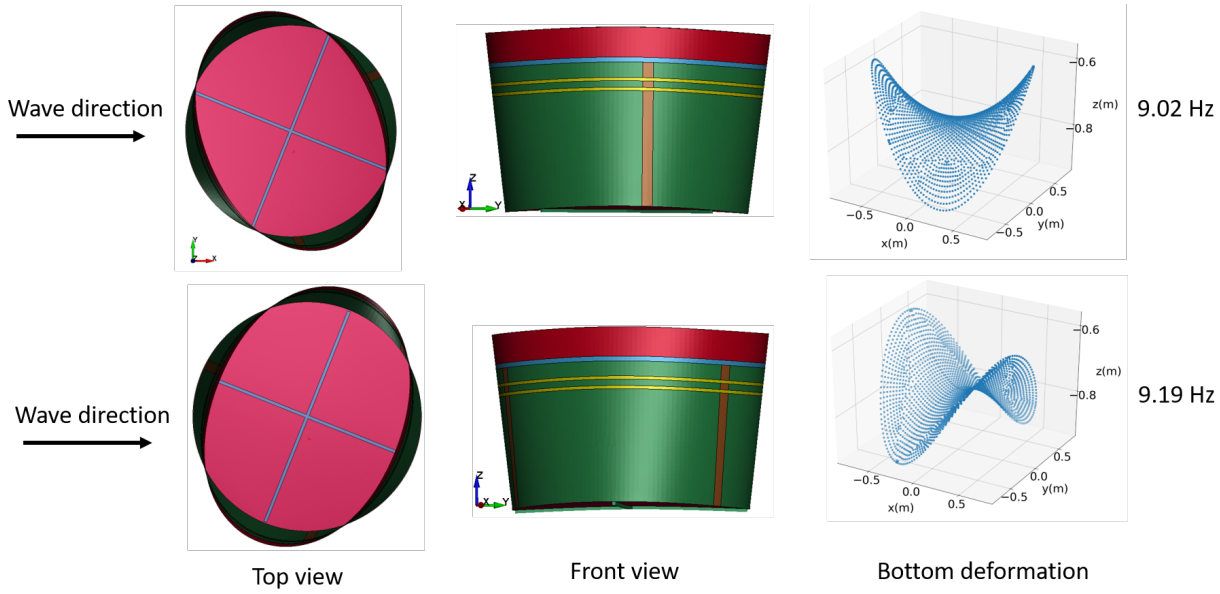

Figure 23: Modal shapes computed in LS-DYNA for the first two orthogonal modes from the eigen-value analysis with dry model. Upper: mode with eigen-frequency 9.02 Hz. Lower: mode with eigen-frequency 9.19 Hz. Left: top view. Middle: front view. Right: deformation mode for the bottom of the cage.

485 influence of sloshing on the corresponding generalized added mass. A numerical analysis of the ovalizing modes has been attempted by combining a FEM software LS-DYNA (Hallquist, 2007) with WAMIT. The implemented FEM structural model is based on the left of Figure 2, with only shell elements used. The aluminum rings with D=20 mm are approximated with plane shell elements of 15.5 mm to hit the first two experimentally obtained dry natural frequencies. The presence of the thin plastic floater is neglected 490 in the FEM model. The influence of the H60 Divinicell is neglected as it's tensile/compressive modulus is significantly smaller than that of PVC.

The numerical model includes the hydroelastic response by including the structural modes calculated by eigen value analysis in absence of liquid. Here we have neglected the effect of water on the mode shapes. Added mass and damping terms for the flexible modes, as well as their coupling with rigid modes, are 495 included in the total added mass and damping matrices. Hence, the linear hydrodynamic coupling between rigid and flexible modes has been modelled. The first two orthogonal modes are relevant for the ovalizing deformations and are used as generalized modes in WAMIT, hence the matrices have a 8X8 dimension, i.e. 6 rigid plus 2 flexible modes. Generalized mass and stiffness matrices from the eigen value analysis of the dry model are included in the equation system. The modal shapes of the first two orthogonal modes are 500 shown in Figure 23. The predicted radial ovalizing deformations are presented in Figure 21. The resonant frequencies in model tests are captured relatively well by the numerical model. The response amplitudes are also well predicted, except in the resonant region, with an obvious overestimation. A possible reason for the overestimation could be due to the free-surface nonlinearities in the experiments.

The current numerical method in frequency domain is a practical approach for the initial design stage to have a good overview of the hydroelatic response of a fish cage in a wide frequency range, with small computational cost. However, if nonlinear sloshing is present, a time domain simulation approach must be considered in which free surface nonlinearity is adopted at least in the internal domain.

4.4. Transfer function of interior waves

Free-surface elevation inside the container was measured by the eight interior wave probes RW1-8, see Figure 1. The probes were installed as fixed to the cage, so the measured values are related to the tank-fixed coordinate system. As an example, transfer functions of the wave probes RW1 and RW4 are provided in Figure 24. The two peaks close to T_{12} and T_{21} are associated with the corresponding natural sloshing modes. In fact, one should note that the coupling between sloshing and body motions affects the natural periods. The maximum values occur at the same wave period as that of the ovalizing modes, i.e., at $\lambda/D = 1.078$. The corresponding time histories of the wave elevation from the regular wave test are shown in Figure 25. The figure clearly shows that the interior wave is still accumulating and more time than examined experimentally is needed to reach steady state. This is similar as that shown in Figure 22 for the elastic deformations. Also in this case, it leads to unrealistic large error bars for the transfer functions, not presented in Figure 24.

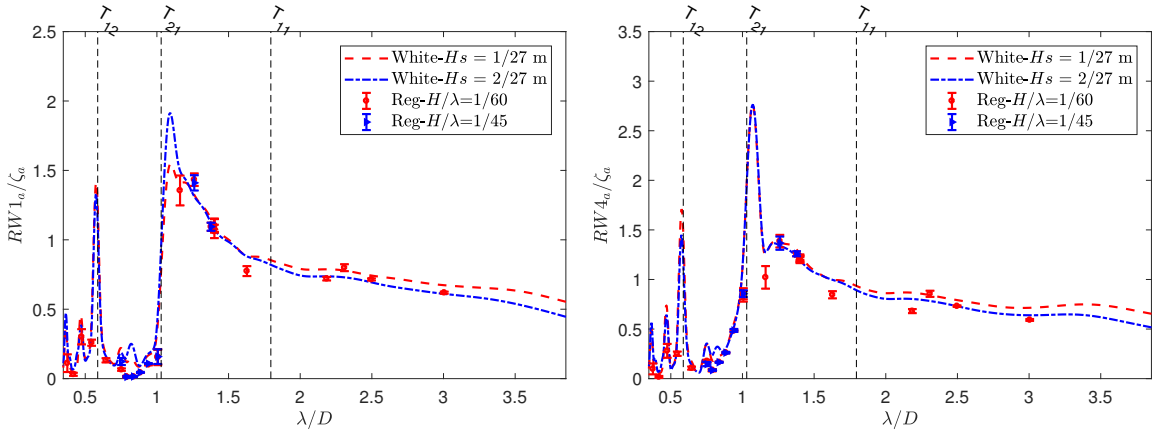

Figure 24: Transfer function of interior wave elevation for the wave probes RW1 and RW4. T_{11} and T_{12} = natural sloshing periods associated with $\cos\theta$ and $\sin\theta$ free-surface mode dependence. T_{21} = natural sloshing period associated with $\cos 2\theta$ and $\sin 2\theta$ free-surface mode dependence.

To better relate the interior wave elevation with sloshing modes, the Fourier components $\cos m\theta$ and $\sin m\theta$ of the internal waves are calculated at $r = 0.95R$, based on the method explained in Section 3.2. Transfer functions of the first three $\cos m\theta, m = 0, 1, 2$ modes and the first two $\sin m\theta, m = 1, 2$ modes are presented in Figure 26. Relevant sloshing natural periods for different modes are indicated by the vertical dashed lines. There is only a $\cos\theta$ component according to linear rigid-body theory. Numerical prediction from WAMIT for $\cos\theta$ mode is also provided and good agreement with the experimental results is observed especially for shorter waves ($\lambda/D < 1.5$). The modes $\cos\theta$ and $\sin\theta$ are 90° out of phase at resonance, which

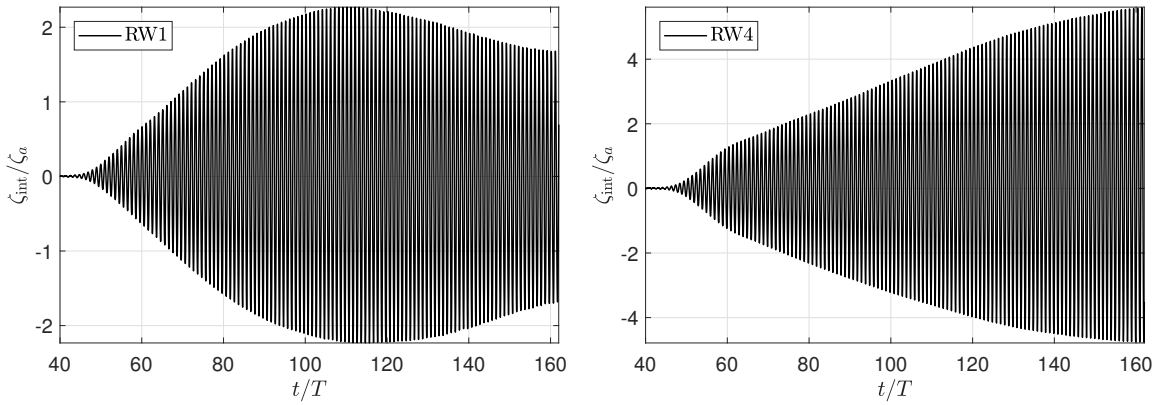

Figure 25: Time histories of internal wave elevation from the wave probes RW1 and RW4 for $T = 1.02$ s, $H = 0.027$ m and $\lambda/D = 1.08$.

implies swirling. However, we note the dominant contribution of the $\cos 2\theta$ and $\sin 2\theta$ terms at resonance and the corresponding phase difference is 180°. The phase difference is evaluated based on the approach introduced in Section 3.3. The fact that the $\sin 2\theta$ mode occurs is associated with structural asymmetry and free-surface nonlinearities. The interior wave elevations associated with the ovalizing deformations are also evaluated based on the hydroelasticity analysis introduced in section 4.3 and are presented in the bottom of Figure 26. Similar as that for the ovalizing deformations, the numerical tool can provide a reasonable prediction of the interior wave amplitudes, but not in the resonant region, with a clear overestimation at the resonant period.

4.5. Mean wave drift forces

When interacting with the cage, the incident waves will cause mean drift loads on the cage due to the far-field waves generated by the structure. The mean surge force is of particular interest as it is important for a mooring analysis. Two methods are pursued to estimate the mean wave-drift force in surge: (1) from tension measurement of the mooring lines; (2) by multiplying the mean surge motion with the equivalent linear stiffness k_s of the system documented in Section 2.2. In the left plot of Figure 27 we present the time histories of the surge force from the two methods for $T = 1.25$ s, $H = 0.041$ m and $\lambda/D = 1.628$. The two strategies yield similar results when the cage is freely floating, without incoming waves ($t < 40T$). A possible reason that the cage has nonzero surge motion in still water is that the time interval between two sucessive tests was not long enough to dampen out the slowly-varying surge motion. Larger differences are observed for both the mean value and amplitude when the cage interacts with the incident waves. The possible reasons for the differences are: (1) the model was moored by four horizontal mooring lines which were attached directly to horizontal free-hanging coil springs. The length of the mooring lines was quite long (about 33 m in model scale), so the weight of the springs will influence the measured forces; (2) videos from the tests show that part of the mooring lines got wet during the tests in waves; (3) cage deformations would also influence the mooring loads. However, the large amplification of the $\cos 2\theta$ and $\sin 2\theta$ response at

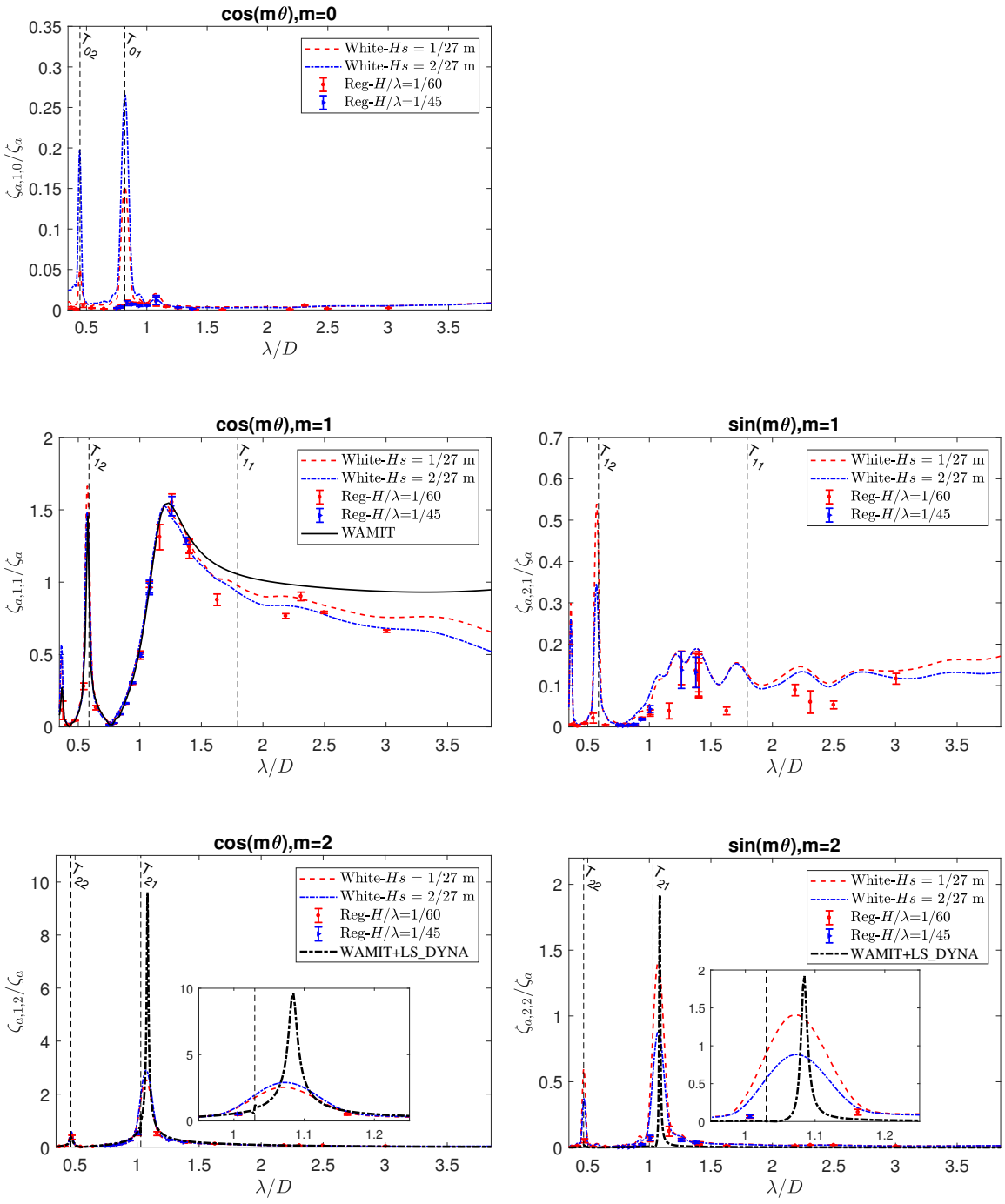

Figure 26: Interior-wave modes $\cos m\theta$ and $\sin m\theta$. Top: $m = 0$. Middle: $m = 1$. Bottom: $m = 2$. Results from WAMIT for $\cos\theta$, $\cos 2\theta$ and $\sin 2\theta$ modes are also provided for comparison. A zoomed view at the resonant zone is also provided for the ovalizing modes. T_{m1} and T_{m2} = natural sloshing periods associated with $\cos m\theta$ and $\sin m\theta$ free-surface mode dependence.

resonance (see Figure 21) indicates small wave radiation due to cage deformation and thereby small influence on the wave drift force. In the right of Figure 27, we shows the comparison of the mean surge forces from the regular wave tests with those from WAMIT. Irregular wave periods, corresponding to eigenperiods for the interior problem with zero Dirichlet condition on the body boundary condition, are suppressed in WAMIT results. The kink at $\lambda/D = 0.58$ is associated with the sloshing natural period T_{12}, as shown in Figure 13. The experimental values are estimated by multiplying the mean surge motion with equivalent stiffness. The evaluation based on the measurement of mooring forces was also performed, but the obtained values were quite scattered, so they are not shown. The asymptotic value of $\bar{F}_1/\rho g\zeta_a^2 D$ is 1/3 for $\lambda/D \to 0$, according to second-order potential flow theory. This is in good agreement with WAMIT.

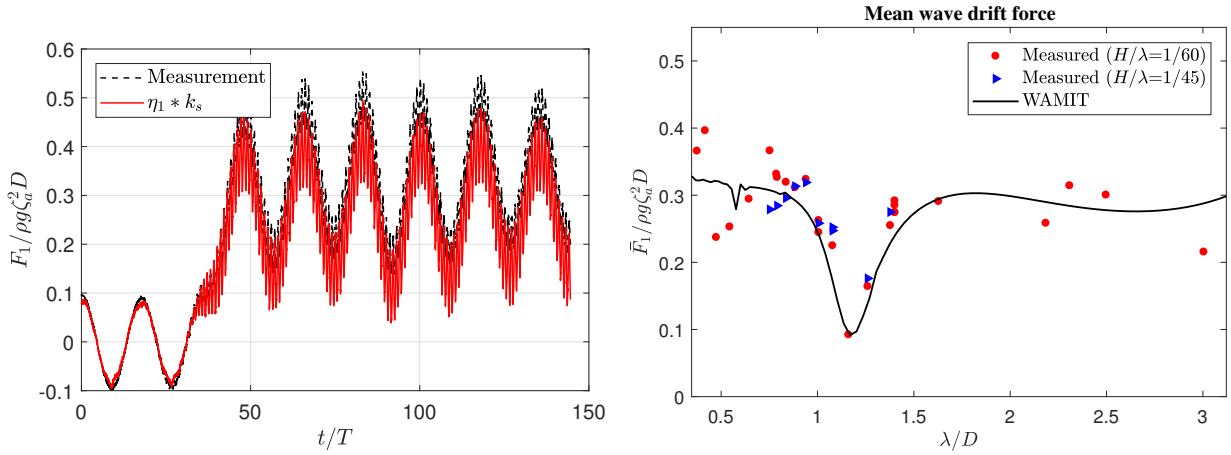

Figure 27: Left: time history of the force acting on the cage in surge. Dashed line: from force measurement. Solid line: from surge motion η_1 multiplied with system stiffness k_s. Right: Non-dimensional mean wave drift force $\bar{F}_1$ in surge versus λ/D. Solid symbols: from regular wave tests. Solid line: from WAMIT. Dashed line: theoretical irregular periods.

5. Conclusions

In this paper, we presented a scaled experimental study of a closed floating cage in waves. The tests were performed in an ocean basin to avoid possible reflections from side tank walls. A main purpose was to investigate how sloshing would influence the global response of the cage, the interior wave elevation and also the mean drift loads. The model was tested in both regular waves and truncated white noise waves. A focus was on the transfer functions in the wave period region associated with local wind generated waves. The radial elastic deformations of the cage were extracted from the measurements of the eight markers installed on the freeboard and relatively large ovalizing radial deformations were observed for wave periods close to the natural sloshing period T_{21} associated with the sloshing modes having a $\cos 2\theta$ and $\sin 2\theta$ dependence. The Fourier modes of the interior wave were also evaluated based on the wave elevations of the eight internal wave probes. The $\cos 2\theta$ and $\sin 2\theta$ modes were found to be dominant and the resonance period coincided with that for the ovalizing radial deformations. The above results imply that hydroelasticity matters and a

non-dimensional parameter involving Young's modulus should be introduced to scale the model test results to full scale. A rational numerical hydroelastic method can be a useful tool in the scaling and requires further studies.

Numerical predictions from the linear potential flow solver WAMIT were also provided, assuming a rigid body. Good agreements between the numerical and experimental results were obtained for both the rigid body motions and corresponding interior wave elevation. Actually, linear potential flow theory can provide a good description of the interior sloshing if the structure is rigid and the coupled natural frequency between surge, pitch and sloshing $\omega_{\text{coupl},1}$ is not close to the lowest natural sloshing frequency ω_1, as it is the case in the present paper.

Nice agreement was also achieved between the numerical predictions and experimental results for the mean drift forces, despite large ovalizing radial modes involved. It seems that the mean wave forces are not so influenced by the elastic deformations of the body and a reliable mooring force analysis can still be performed, neglecting body elasticity. A numerical analysis of the ovalizing modes was also attempted by combining the structural analysis program LS-DYNA with WAMIT. The resonant frequencies in model tests were well captured. In terms of the ovalizing deformations and interior waves, the proposed numerical tool could provide reasonable predictions, except in the resonant zone where the free-surface nonlinearities may matter, with a clear overestimation from the linear results.

In the present study, a torus-shaped floater was applied to increase the static stability of the cage in roll and pitch. From the model tests, the floating collar can easily go in and out water due to small draft, causing parametric pitch instability in long waves and consequently large pitch motion. To avoid such drawback, a floater with much larger draft is suggested, so to avoid a time-dependent change of the restoring stiffness and consequently prevent instability.

Acknowledgement

This work was supported by the Research Council of Norway through the Centers of Excellence funding scheme AMOS, project number 223254.

The authors acknowledge Andrei Tsarau from Sintef Ocean for providing the experimental data. The experiments were conducted by Reza Firoozkoohi and Stefan Arenfeldt Vilsen at Sintef Ocean. The financial support for the experiments by the Research Council of Norway (grant no. 268402), the Norwegian Seafood Research Fund and the industry partners through the project "Safe operation of closed aquaculture cages in waves is also appreciated.

References

Bendat, J.S., Piersol, A.G., 2011. Random data: analysis and measurement procedures. volume 729. John Wiley & Sons.

Faltinsen, O.M., Timokha, A.N., 2009. Sloshing. Cambridge University Press.

Faltinsen, O.M., Timokha, A.N., 2021. Coupling between resonant sloshing and lateral motions of a two-dimensional rectangular tank. Journal of Fluid Mechanics .

Ghamari, I., Greco, M., Faltinsen, O.M., Lugni, C., 2020. Numerical and experimental study on the parametric roll resonance for a fishing vessel with and without forward speed. Applied Ocean Research 101, 102272.

Hallquist, J.O., 2007. LS-DYNA keyword user's manual. Livermore Software Technology Corporation 970.

Hansen, E.W., 2014. Fourier transforms: principles and applications. John Wiley & Sons.

Harris, F.J., 1978. On the use of windows for harmonic analysis with the discrete Fourier transform. Proceedings of the IEEE 66, 51–83. doi:10.1109/PROC.1978.10837.

Haslum, H., Faltinsen, O.M., 1999. Alternative shape of spar platforms for use in hostile areas, in: Offshore technology conference, Offshore Technology Conference.

Kim, Y., Nam, B., Kim, D., Kim, Y., 2007. Study on coupling effects of ship motion and sloshing. Ocean Engineering 34, 2176–2187.

Klotter, K., 2013. Technische Schwingungslehre: Erster Band: Einfache Schwinger. Springer-Verlag.

Kristiansen, D., Lader, P., Endresen, P.C., Aksnes, V., 2018. Numerical and experimental study on the seakeeping behavior of floating closed rigid fish cages, in: International Conference on Offshore Mechanics and Arctic Engineering, American Society of Mechanical Engineers. p. V006T05A001.

Lader, P., Fredriksson, D.W., Volent, Z., DeCew, J., Rosten, T., Strand, I.M., 2017. Wave response of closed flexible bags. Journal of Offshore Mechanics and Arctic Engineering 139.

Lee, C.H., 1995. WAMIT theory manual. Massachusetts Institute of Technology, Department of Ocean Engineering.

Malenica, S., Zalar, M., Chen, X., 2003. Dynamic coupling of seakeeping and sloshing, in: The Thirteenth International Offshore and Polar Engineering Conference, International Society of Offshore and Polar Engineers.

Newman, J., 2005. Wave effects on vessels with internal tanks, in: Proceedings of the 20th Workshop on Water Waves and Floating Bodies, Spitsbergen, Norway.

Oppenheim, A.V., Buck, J.R., Schafer, R.W., 2001. Discrete-time signal processing. Vol. 2. Upper Saddle River, NJ: Prentice Hall.

Rognebakke, O.F., Faltinsen, O.M., 2003. Coupling of sloshing and ship motions. Journal of Ship Research 47, 208–221.

Shen, Y., Marilena, G., Faltinsen, O.M., Ma, S., 2020. Numerical study towards closed fish farms in waves using two harmonic polynomial cell methods, in: Proceedings of the 35th International Workshop on Water Waves and Floating Bodies, Seoul, Korea, pp. 141–144.

StandardNorge, 2009. Marine fish farms - requirements for site survey risk, analysis, design, dimensioning, production,installation and operation, NS 9415.

Strand, I.M., Faltinsen, O.M., 2019. Linear wave response of a 2D closed flexible fish cage. Journal of Fluids and Structures 87, 58–83.

Strand, I.M., Faltinsen, O.M., 2020. Linear wave-induced dynamic structural stress analysis of a 2d semi-flexible closed fish cage. Journal of Fluids and Structures 94, 102909.

Welch, P., 1967. The use of fast Fourier transform for the estimation of power spectra: a method based on time averaging over short, modified periodograms. IEEE Transactions on audio and electroacoustics 15, 70–73.

Zhao, R., Faltinsen, O.M., Krokstad, J., Aanesland, V., 1988. Wave-current interaction effects on large-volume structures, in: Proceedings of the International Conference on the Behavior of Offshore Structures (BOSS'88), Trondheim, Norway, pp. 623–638.